



HAL
open science

Spatially resolved properties of early-type group-dominant galaxies with MUSE: gas content, ionization mechanisms, and metallicity gradients

P. Lagos, S. I. Loubser, T. C. Scott, E. O'Sullivan, K. Kolokythas, A. Babul, A. Nigoche-Netro, V. Olivares, C. Sengupta

► To cite this version:

P. Lagos, S. I. Loubser, T. C. Scott, E. O'Sullivan, K. Kolokythas, et al.. Spatially resolved properties of early-type group-dominant galaxies with MUSE: gas content, ionization mechanisms, and metallicity gradients. *Monthly Notices of the Royal Astronomical Society*, 2022, 516, pp.5487-5506. 10.1093/mnras/stac2535 . insu-03851595

HAL Id: insu-03851595

<https://insu.hal.science/insu-03851595>

Submitted on 24 Mar 2023

HAL is a multi-disciplinary open access archive for the deposit and dissemination of scientific research documents, whether they are published or not. The documents may come from teaching and research institutions in France or abroad, or from public or private research centers.

L'archive ouverte pluridisciplinaire **HAL**, est destinée au dépôt et à la diffusion de documents scientifiques de niveau recherche, publiés ou non, émanant des établissements d'enseignement et de recherche français ou étrangers, des laboratoires publics ou privés.

Spatially resolved properties of early-type group-dominant galaxies with MUSE: gas content, ionization mechanisms, and metallicity gradients

P. Lagos ^{1,2}★ S. I. Loubser ^{2,3}★ T. C. Scott ¹★ E. O’Sullivan ⁴ K. Kolokythas ² A. Babul,⁵
A. Nigoche-Netro,⁶ V. Olivares ^{7,8} and C. Sengupta ⁹

¹*Instituto de Astrofísica e Ciências do Espaço, Universidade do Porto, CAUP, Rua das Estrelas, P-4150-762 Porto, Portugal*

²*Centre for Space Research, North-West University, Potchefstroom 2520, South Africa*

³*National Institute for Theoretical and Computational Sciences (NITheCS), Potchefstroom 2520, South Africa*

⁴*Center for Astrophysics | Harvard & Smithsonian, 60 Garden Street, Cambridge, MA 02138, USA*

⁵*Department of Physics and Astronomy, University of Victoria, Victoria, BC V8W 2Y2, Canada*

⁶*Instituto de Astronomía y Meteorología, Av. Vallarta 2602. Col. Arcos Vallarta. Guadalajara, Jalisco C.P. 44130, México*

⁷*LERMA, Observatoire de Paris, PSL Research Univ., CNRS, Sorbonne Univ., F-75014 Paris, France*

⁸*Department of Physics and Astronomy, University of Kentucky, 505 Rose Street, Lexington, KY 40506, USA*

⁹*Purple Mountain Observatory, No. 8 Yuanhua Road, Qixia District, Nanjing 210034, China*

Accepted 2022 August 22. Received 2022 July 25; in original form 2022 February 4

ABSTRACT

With the goal of a thorough investigation of the ionized gas and its origin in early-type group-dominant galaxies, we present archival MUSE data for 18 galaxies from the Complete Local-Volume Groups Sample (CLoGS). These data allowed us to study the spatially resolved warm gas properties, including the morphology of the ionized gas, $\text{EW}(\text{H}\alpha)$, and kinematics as well as the gas-phase metallicity ($12 + \log(\text{O}/\text{H})$) of these systems. In order to distinguish between different ionization mechanisms, we used the emission-line ratios $[\text{O III}]/\text{H}\beta$ and $[\text{N II}]/\text{H}\alpha$ in the BPT diagrams and $\text{EW}(\text{H}\alpha)$. We find that the ionization sources in our sample have variable impacts at different radii; central regions are more influenced by low-luminosity active galactic nuclei, while extended regions of low-ionization nuclear emission-line region-like emission are ionized by other mechanisms with post-asymptotic giant branch stars photoionization likely contributing significantly. We classified our sample into three $\text{H}\alpha + [\text{N II}]$ emission morphology types. We calculate the gas-phase metallicity assuming several methods and ionization sources. In general, $12 + \log(\text{O}/\text{H})$ decreases with radius from the centre for all galaxies, independently of nebular morphology type, indicating a metallicity gradient in the abundance profiles. Interestingly, the more extended filamentary structures and all extranuclear star-forming regions present shallow metallicity gradients. Within the uncertainties these extended structures can be considered chemically homogeneous. We suggest that group-dominant galaxies in our sample likely acquired their cold gas in the past as a consequence of one or more mechanisms, e.g. gas-clouds or satellite mergers/accretion and/or cooling flows that contribute to the growth of the ionized gas structures.

Key words: galaxies: abundances – galaxies: elliptical and lenticular, cD – galaxies: groups: general – galaxies: ISM – galaxies: nuclei.

1 INTRODUCTION

Most galaxies are found in groups and clusters. The distinction between them is made by the number of their members; clusters have $\gtrsim 50$ member galaxies and are more massive than groups. Bright galaxies at the centres of galaxy groups (hereafter BGGs) or group-dominant galaxies typically have stellar masses of $M_* \gtrsim 10^{10-13} M_\odot$ (e.g. Gozaliasl et al. 2016; O’Sullivan et al. 2018; Kolokythas et al. 2022), with some BGGs also displaying X-ray emission (e.g. O’Sullivan et al. 2017) and containing cold HI and/or molecular gas in the range $\sim 10^{8-10} M_\odot$ (e.g. O’Sullivan et al. 2015, 2018). A significant fraction (~ 25 per cent; Gozaliasl et al. 2016) of BGGs

lie on the main sequence of the star-forming (late-type) galaxies at $z \lesssim 0.4$, and this fraction increases with redshift. However, most BGGs are early-type galaxies (ETGs), i.e. elliptical and/or lenticular (S0) galaxies. Early-type BGGs (e.g. Kolokythas et al. 2022), and many other ETGs in the literature (e.g. Shapiro et al. 2010; Fang et al. 2012; Gomes et al. 2016), contain warm ionized gas and ongoing low-level star formation (SF) ($\text{SFR}_{\text{FUV}} \sim 0.01\text{--}0.4 M_\odot \text{ yr}^{-1}$; Kolokythas et al. 2022), while in late-type BGGs the SF can reach $\sim 10 M_\odot \text{ yr}^{-1}$ (Oliva-Altamirano et al. 2014; Gozaliasl et al. 2016). This same activity is also found in a significant fraction of Brightest Cluster Galaxies (BCGs; e.g. Bildfell et al. 2008; Pipino et al. 2009; McDonald et al. 2010; Donahue et al. 2011; McDonald, Veilleux & Mushotzky 2011; Werner et al. 2014; Loubser et al. 2016).

ETGs (e.g. Phillips et al. 1986; Trinchieri & di Serego Alighieri 1991; Annibali et al. 2010), including some early-

* E-mail: Patricio.Lagos@astro.up.pt (PL); Ilani.Loubser@nwu.ac.za (SIL); tom.scott@astro.up.pt (TCS)

type BGGs,¹ also display low-ionization nuclear emission-line regions (LINERs, Heckman 1980). The spectra of LINERs exhibit strong low-ionization optical emission lines such as [O III] λ 5007, [O II] λ 3726/29, [N II] λ 6584, [S II] λ 6717,6731, and hydrogen Balmer lines ($H\alpha$, $H\beta$, etc), commonly with [N II] λ 6584 > $H\alpha$ emission. Several explanations for LINER emission, in galaxies, have been proposed including shock-ionization (e.g. Heckman 1980; Dopita & Sutherland 1995, 1996; Allen et al. 2008), photoionization by ongoing low-level SF (e.g. Schawinski et al. 2007; Shapiro et al. 2010; Fogarty et al. 2015), hot evolved post-asymptotic giant branch (pAGB) stars (e.g. Binette et al. 1994; Stasińska et al. 2008; Annibali et al. 2010; Cid Fernandes et al. 2010, 2011; Sarzi et al. 2010), photoionization by the ‘cooling’ X-ray-emitting gas (Voit & Donahue 1990; Donahue & Voit 1991; Ferland, Fabian & Johnstone 1994; Voit, Donahue & Slavin 1994; Polles et al. 2021), thermal conduction from the hot gas (Sparks, Macchetto & Golombek 1989), and ionization by low-luminosity active galactic nuclei (AGNs) (e.g. Ferland & Netzer 1983; Barth et al. 1998; Ho 1999). Observational evidence suggests that more than one mechanism are likely to be at work in LINERs (e.g. Edwards et al. 2007; Fogarty et al. 2015, in BCGs). For instance, the contribution of AGNs to the photoionization of LINERs may be restricted to the nuclear region (e.g. Sarzi et al. 2010), while pAGB stars are likely responsible for the extended gas emission (e.g. Binette et al. 1994; Sarzi et al. 2010; Gomes et al. 2016). Extended low-ionization emission-line regions (LIERs; Belfiore et al. 2016) or LINER-like extranuclear diffuse ionized gas (DIG) emission in ETGs has been detected and studied (e.g. Sarzi et al. 2006; Gomes et al. 2016) as part of the SAURON (Bacon et al. 2001) and Calar Alto Legacy Integral Field Area (CALIFA, Sánchez et al. 2012) surveys. These studies suggest low-luminosity AGNs are likely contributing to LINER emission in a less than dominant way (Yan & Blanton 2012).

Extended and DIG filaments are observed in BGGs/BCGs (e.g. Heckman et al. 1989; Crawford et al. 1999; O’Sullivan et al. 2012; Tremblay et al. 2018; Olivares et al. 2019). These ionized gas filaments seem to be co-spatial with large quantities of H I and molecular gas, traced by CO, and soft X-ray emission features (Werner et al. 2014). McDonald et al. (2010) found that the extended warm gas in cluster galaxies, in general, is spatially coincident with cooling intracluster medium (ICM) flows. McDonald et al. (2011) and McDonald, Veilleux & Rupke (2012) rule out collisional ionization by cosmic rays, thermal conduction, photoionization by ICM X-rays, and AGNs as strong contributors to the ionization of the warm gas, in both the nuclei and filaments of cool-core clusters. They argue that the data are adequately described by a composite model of slow shocks and SF. According to McDonald et al. (2011), the $H\alpha$ filaments in BGGs/BCGs are more strongly correlated with the cooling properties of the ICM than with the radio properties of the BCGs. The molecular gas in the filaments is located along old radio jets, lobes, and/or below X-ray cavities, suggesting that AGN activity supplies a regular input of energy in those systems (Russell et al. 2016; O’Sullivan et al. 2021). Generally, the dominant ionization mechanism, as well as their locations (i.e. nuclear and/or extended regions), is not clear and different processes may be at work during the evolution of each type of system.

Hot (10^7 K) gas-phase metallicity is another key property for studying the effect of galactic environments and AGN/SF feedback in groups and clusters (for a review see Gastaldello et al. 2021). The X-ray-emitting intra-group medium (IGrM) shows several emission lines typical of elements synthesized by stars/supernovae (SNe) and

deposited in the IGrM/ICM via galactic winds from the group/cluster members (e.g. Liang et al. 2016), ram-pressure stripping/tidal interactions (Taylor & Babul 2001; McCarthy et al. 2008), and others (for a review see Schindler & Diaferio 2008). Several studies (e.g. Mernier et al. 2017; Gastaldello et al. 2021, and references therein) show that the average abundance profiles of Fe and others elements (e.g. O, Si, Ar) in the ICM/IGrM increase towards the core of cool-core clusters/groups up to values of $\sim 1.0 Z_{\odot}$, and decrease at large radii. This peaked distribution is associated with the release of metals from the galaxy members via mechanical feedback from AGN/SF activity, gas turbulence (Rennehan et al. 2019), or infalling galaxies through ram-pressure stripping across the evolution of the systems. Although some studies (e.g. Werner et al. 2006) report a rather flat O and Mg profiles, non-cool-core clusters and groups do not exhibit clear Fe abundance gradient in their cores. Mechanisms such as merger-induced sloshing motions (O’Sullivan, David & Vrtillek 2014, and references therein) can also transport the released metals from the galaxies into the IGrM/ICM. On the other hand, the spatial distribution of abundances of the warm (10^4 K) gas-phase in the interstellar medium (ISM) of the galaxies is also important for understanding the formation history of these systems. Studies of local star-forming galaxies have shown a negative metallicity gradient (the metallicity decreases radially) with increasing galactocentric radius (e.g. Martin & Roy 1992; van Zee et al. 1998, among many others). However, this radial distribution can present deviations from this simple negative gradient, namely a steep decrease of oxygen abundance ($12 + \log(O/H)$) in the nuclear regions and a flattening of the gradient in the outer parts (see Sánchez-Menguiano et al. 2018; Sánchez 2020, and references therein). Several mechanisms have been proposed to explain these features such as radial migration, infall of gas, or satellite accretion. In early-type group-dominant galaxies, the presence of these features and the origin of their gas are poorly understood (e.g. Annibali et al. 2010). The cold gas in group and cluster ETGs potentially originates from two main sources: internal production (a large fraction of stellar mass is believed to be released in the form of cold gas, Davis et al. 2011) and external accretion, i.e. mergers, stripping gas from satellites, gas from the IGrM/ICM (e.g. Jung et al. 2022). A kinematical decoupling between gas and stars as evidence for external gas origin was found in many ETGs in the SAURON (Sarzi et al. 2006, 2010) and CALIFA (Gomes et al. 2016) surveys.

Complete Local-Volume Groups Sample (CLoGS) (O’Sullivan et al. 2017) is an optically selected sample of 53 groups at distances of less than 80 Mpc and is the first statistically complete sample of nearby galaxy groups studied with an extensive multiwavelength data set, including X-ray (*Chandra* and *XMM-Newton*; O’Sullivan et al. 2017), radio (GMRT and VLA; Kolokythas et al. 2018, 2019), and sub-mm (IRAM-30m and APEX; O’Sullivan et al. 2018) observations. In addition, we have analysed spatially resolved long-slit spectroscopy from the 10m Hobby–Eberly Telescope (van den Bosch et al. 2015) for a subsample of 23 of the CLoGS dominant central galaxies (see Loubser et al. 2018). Archival *GALEX* FUV and *WISE* photometry for the group-dominant galaxies are presented in Kolokythas et al. (2022). In this paper, we use archival optical ESO Very Large Telescope (VLT) Integral Field Unit (IFU) Multi-Unit Spectroscopic Explorer (MUSE) observations of a sample of 18 early-type group-dominant CLoGS galaxies. We aim to investigate the relation between the properties (i.e. emission-line ratios, chemical abundances, etc.) and structure of each galaxy’s ISM in order to constrain the ionization processes, the origin of their gas, and its chemical abundance distribution. In related papers, using the same MUSE data set, Olivares et al. (2022) present a detailed analysis of the ionized gas kinematics, while in Loubser et al. (2022) we study the stellar

¹See the list of galaxies in this paper.

Table 1. General parameters of our sample and observing log. Column (1) gives the galaxy name, Column (2) the morphology, Columns (3) and (4) give their coordinates, Column (5) presents the galactic extinction A_V (mag) (Schlafly & Finkbeiner 2011), and Columns (6) and (7) give the distance and redshift, respectively. D (Local Group) and z from NED assuming $H_0 = 73.0 \text{ km s}^{-1} \text{ Mpc}^{-1}$. In Column (8) we give X-ray morphology (extent of the gas halo) and core type as cool-core/non-cool-core (CC/NCC) based on their temperature profiles (O’Sullivan et al. 2017) for systems where thermal emission was detected: group-like (GRP, extent $>65 \text{ kpc}$), galaxy-like (gal, extent $\sim 10\text{--}65 \text{ kpc}$), and point-like (pnt, unresolved, extent smaller than the *XMM-Newton* PSF). Radio morphology (Kolokythas et al. 2018): point-like (pnt, radio source with sizes $\lesssim 11 \text{ kpc}$), diffuse emission (diffuse, with no clear jet or lobe structure), small-scale jets (jet, $<20 \text{ kpc}$ jets confined within the stellar body of the host galaxy), and large-scale jets (JET, $>20 \text{ kpc}$ jets extending beyond the host galaxy and into the IGrM). Finally, Columns (9)–(11) show the observation date, exposure time, and mean airmass during the observations, respectively.

Name	Morphology	RA	Dec.	A_V	D	z	X-ray/radio	Date	Exp. time	Mean
(1)	(2)	(J2000)	(J2000)	(mag)	(Mpc)	(7)	morphology	of observation	(s)	airmass
(1)	(2)	(3)	(4)	(5)	(6)	(7)	(8)	(9)	(10)	(11)
NGC 193	E	00 ^h 39 ^m 18.6 ^s	+03 ^d 19 ^m 52 ^s	0.062	62.7	0.014723	GRP (CC) / JET	2016-06-08	3 × 900	1.524
NGC 410	E	01 ^h 10 ^m 58.9 ^s	+33 ^d 09 ^m 07 ^s	0.161	75.8	0.017659	GRP (CC) / pnt	2016-08-16	3 × 900	1.937
NGC 584	E	01 ^h 31 ^m 20.7 ^s	−06 ^d 52 ^m 05 ^s	0.116	25.9	0.006011	.../ pnt	2016-07-01	3 × 900	1.243
NGC 677	E	01 ^h 49 ^m 14.0 ^s	+13 ^d 03 ^m 19 ^s	0.243	71.9	0.017012	GRP (CC) / diffuse	2016-07-20	3 × 900	1.344
NGC 777	E	02 ^h 00 ^m 14.9 ^s	+31 ^d 25 ^m 46 ^s	0.128	71.4	0.016728	GRP (NCC) / pnt	2016-08-16	3 × 900	1.823
NGC 924	S0	02 ^h 26 ^m 46.8 ^s	+20 ^d 29 ^m 51 ^s	0.467	63.1	0.014880	.../ pnt	2016-08-14	3 × 900	1.651
NGC 940	S0	02 ^h 29 ^m 27.5 ^s	+31 ^d 38 ^m 27 ^s	0.246	72.6	0.017075	pnt / pnt	2016-08-21	3 × 900	1.814
NGC 978	E/S0	02 ^h 34 ^m 47.6 ^s	+32 ^d 50 ^m 37 ^s	0.253	67.3	0.015794	gal (NCC) / pnt	2016-08-16	3 × 900	1.866
NGC 1060	E/S0	02 ^h 43 ^m 15.0 ^s	+32 ^d 25 ^m 30 ^s	0.532	73.4	0.017312	GRP (CC) / jet	2016-08-22	3 × 900	1.845
NGC 1453	E	03 ^h 46 ^m 27.2 ^s	−03 ^d 58 ^m 08 ^s	0.289	52.9	0.012962	GRP (NCC) / pnt	2016-07-22	3 × 900	1.358
NGC 1587	E	04 ^h 30 ^m 39.9 ^s	+00 ^d 39 ^m 42 ^s	0.197	50.0	0.012322	GRP (NCC) / diffuse	2016-08-18	3 × 900	1.360
NGC 4008	E	11 ^h 58 ^m 17.0 ^s	+28 ^d 11 ^m 33 ^s	0.064	49.0	0.012075	gal (NCC) / pnt	2016-05-13	3 × 900	1.668
NGC 4169	S0	12 ^h 12 ^m 18.8 ^s	+29 ^d 10 ^m 46 ^s	0.058	51.4	0.012622	pnt / pnt	2016-05-19	3 × 900	1.728
NGC 4261	E	12 ^h 19 ^m 23.2 ^s	+05 ^d 49 ^m 31 ^s	0.049	28.4	0.007378	GRP (CC) / JET	2016-04-17	3 × 880	1.311
ESO0507-G025	E/S0	12 ^h 51 ^m 31.8 ^s	−26 ^d 27 ^m 07 ^s	0.245	41.1	0.010788	.../ diffuse	2016-04-12	3 × 900	1.107
NGC 5846	E	15 ^h 06 ^m 29.3 ^s	+01 ^d 36 ^m 20 ^s	0.153	23.1	0.005711	GRP (CC) / jet	2016-05-16	3 × 880	1.579
NGC 6658	S0	18 ^h 33 ^m 55.6 ^s	+22 ^d 53 ^m 18 ^s	0.339	61.6	0.014243	pnt / ...	2016-04-23	3 × 870	1.557
NGC 7619	E	23 ^h 20 ^m 14.5 ^s	+08 ^d 12 ^m 22 ^s	0.224	54.6	0.012549	GRP (CC) / pnt	2016-05-23	3 × 870	1.444

kinematics of the fast and slow rotators in this sample. The paper is organized as follows: Section 2 contains the technical details regarding the observations, data reduction, spectral fitting, and measurement of line fluxes; Section 3 describes our results on the structure and physical properties of the ionized gas; Section 4 discusses the results. Finally, in Section 5 we summarize our conclusions. Appendices are available as supplementary online material. In the following analysis, we adopt as solar abundances $Z_{\odot} = 0.0142$, $X_{\odot} = 0.7154$, and $[12 + \log(\text{O}/\text{H})]_{\odot} = 8.69$ from Asplund et al. (2009).

2 THE DATA AND EMISSION-LINE MEASUREMENTS

2.1 Observations and data reduction

Our sample consists of 18 group-dominant galaxies selected from the CLoGS nearby groups sample (O’Sullivan et al. 2017). Each galaxy has archival ESO VLT/MUSE (Bacon et al. 2010) data. Four of our targets were previously observed in the CALIFA IFU survey (NGC 677, NGC 924, NGC 1060, and NGC 7619). The observations (program ID 097.A-0366(A)) were made with the MUSE spectrograph, which used the Nasmyth B focus on Yepun the 8.2m VLT UT4. The observations were made in the wide field mode over a $1 \text{ arcmin} \times 1 \text{ arcmin}$ Field of View (FoV) sampled by a system of 24 spectrographs with an spectral coverage between ~ 4800 and 9300 \AA , a spectral resolution of $\sim 2.6 \text{ \AA}$, spectral sampling of 1.25 \AA , and spatial sampling of 0.2 arcsec per spaxel, leading to a total of 90 000 spectra per exposure. For each galaxy three exposures were taken. These observations were dithered with a few arcsecond dither pattern in order to cover a large portion of each galaxy’s ISM. Offset sky observations were used for sky subtraction. In Table 1,

we show the general parameters for the sample members and the observation log.

The data were reduced using the MUSE pipeline (v2.6.2, Weilbacher et al. 2020), with steps including bias correction, wavelength calibration, construction of data cubes from the individual spectra from the detectors, correction of the spectra to the heliocentric frame, skysubtraction, and merging of the individual exposures to form a combined data cube with a total of $\sim 200\,000$ spectra per each galaxy. Finally, the data cubes were corrected for redshift and galactic extinction using the reddening function given by Cardelli, Clayton & Mathis (1989). In Fig. 1, we show the nuclear spectra of each member of our sample. More details in Section 2.2.

2.2 Spectral fitting and emission-line measurement

We fitted and removed the stellar component within each spectrum (bin or spaxel), in order to obtain pure emission line spectra using the spectral synthesis code Fitting Analysis using Differential evolution Optimization (FADO, Gomes & Papaderos 2017) version V1.B. Simple stellar population (SSP) templates from the Bruzual & Charlot (2003) libraries were used with metallicities between $Z = 0.004$ and $Z = 0.05$ and stellar ages between 1 Myr and 15 Gyr, for a Chabrier initial mass function (IMF, Chabrier 2003). FADO self-consistently reproduces the nebular characteristics of a galaxy, including the hydrogen Balmer-line luminosities, equivalent widths (EWs), and nebular continuum. An important advantage of FADO is that its convergence scheme employs genetic differential evolution optimization. This results in improvements with respect to the uniqueness of spectral fits and the overall efficiency of the convergence schemes. Artificial intelligence is used to eliminate redundancies in the SSP base libraries which increases the computational efficiency. The fit was performed in the $4800\text{--}7000 \text{ \AA}$ spectral range assuming the

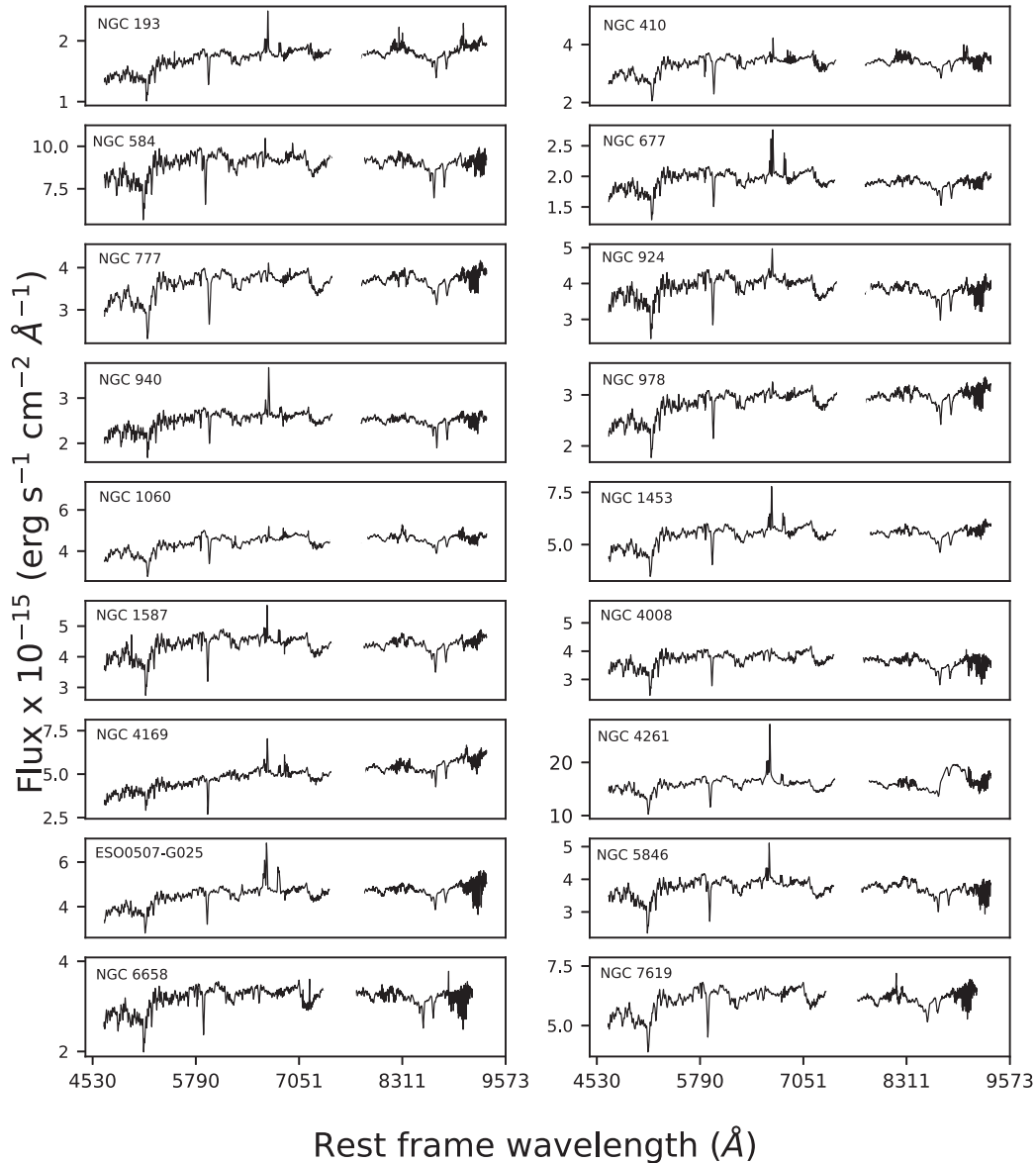


Figure 1. Observed MUSE spectra for our sample of group-dominant galaxies extracted from a nuclear 3 arcsec aperture and covering the entire MUSE wavelength range.

Cardelli et al. (1989) extinction law. The data cubes were tessellated using the Voronoi binning method (Cappellari & Copin 2003) to achieve an adequate signal to noise (S/N; we choose a $S/N \sim 30\text{--}50$) per bin for the continuum between 6000 and 6200 Å. The Voronoi binning method lead to the dilution of the emission lines within the bins, so the shape of extended and diffuse emission lines was lost (see Erroz-Ferrer et al. 2019, for a similar approach). Then, the best-fitting stellar continuum or synthetic Spectral Energy Distribution (SED) was subtracted from the observed spaxels, with $S/N > 3$ in the continuum, to obtain pure emission-line data cubes. FADO provides as results, among others, mass contributions of individual stellar populations, mass- and luminosity-weighted stellar ages and metallicities, emission-line fluxes, EWs, FWHMs, and estimates of their uncertainties. In Fig. 2, we show an example to illustrate the spectral modelling results with FADO from a nuclear 3 arcsec aperture for the galaxy ESO0507-G025. In order to test the accuracy of these results, we carried out a single-Gaussian fit to each emission

line. Our fit results were in good agreement with those from FADO, consequently for the analysis in this study we create the following emission-line maps using FADO: $H\alpha$, $H\beta$, $[O\text{ III}] \lambda 5007$, $[N\text{ II}] \lambda 6584$, and $[S\text{ II}] \lambda\lambda 6717, 6731$. We note that, when deriving the maps, we only use spaxels with emission fluxes $> 3\sigma$ above the background. We did not detect significant broad asymmetric emission-line profiles, so multiple-component decomposition of the emission lines was not necessary, because each emission line is well described by a single Gaussian profile. More details about the morphologies of these maps is given in Section 3.1.

Following a similar procedure to Parkash et al. (2019), we extracted for each galaxy a spectrum from a circular region at the galaxy continuum centre with a diameter of 3 arcsec in order to mimic the SDSS spectral fibre aperture. From here on we refer to this circular region as the nuclear region and the spectra from this region as the nuclear spectrum (see Fig. 1). The nuclear spectra of the galaxies are characterized by the presence of strong $[N\text{ II}] \lambda 6584$ emission with

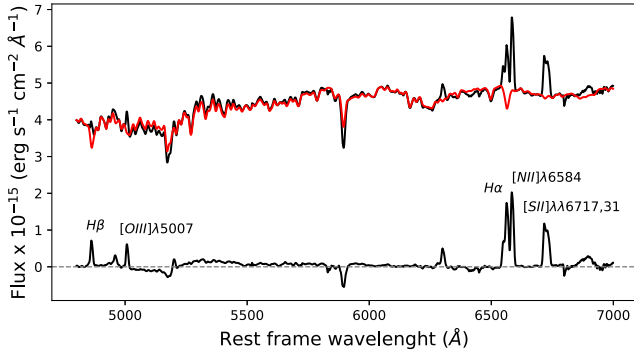


Figure 2. Example of the stellar continuum fit modelling with FADO for the galaxy ESO0507-G025 from the nuclear 3 arcsec aperture. The black and red upper lines correspond to the observed and modelled stellar spectrum, respectively. By subtracting the latter from the former we obtain the pure nebular emission line spectrum (lower black line). We have labelled the emission lines used in our analysis.

$[\text{N II}] \lambda 6584 / \text{H}\alpha > 1$, which is consistent with LINERs. Additionally, we extracted an integrated spectrum for each galaxy within an aperture which encompasses the extended emission in Fig. 3 (see Section 3.1.1) with $[\text{N II}] \lambda 6584$ emission $> 3\sigma$ per pixel. In summary, we find 15/18 objects with intensive nuclear ionized-gas (LINERs) with $[\text{N II}] \lambda 6584 > \text{H}\alpha$. Pagotto et al. (2021) found the strongest and most spatially extended emission, in their sample of massive ETGs in densest clusters of galaxies, came from the $[\text{N II}] \lambda 6584$ lines. We find the same result for our sample. In Table 2, we present for each galaxy the 3 arcsec nuclear and integrated observed $F(\text{H}\alpha)$ flux, $F(\text{H}\alpha)/F(\text{H}\beta)$ multiplied by a factor of 100, $F([\text{N II}] \lambda 6584)$ flux, and $\text{EW}(\text{H}\alpha)$, respectively. We note that using the spectral synthesis code FADO (Gomes & Papaderos 2017) and the Bruzual & Charlot (2003) stellar spectral library, we resolved weak $[\text{O III}] \lambda 5007$, $\text{H}\beta$, $\text{H}\alpha$, and $[\text{N II}] \lambda 6584$ emission in the nuclear region of NGC 6658. However, Olivares et al. (2022) using pPXF (Cappellari 2017) and the Indo-U.S. Coudé Feed stellar library (Valdes et al. 2004) find no emission lines in the spectrum of this galaxy using the same MUSE data set. The results for this galaxy are therefore uncertain, especially given that no clear emission line peaks are observed in the integrated spectrum.

Finally, we explored the data cubes of our target BGGs (see Appendix A available as supplementary online material) in order to find additional emission line galaxies in the FoV. We found two additional objects in the FoV of NGC 677 and one in the FoVs of NGC 777, NGC 924, and NGC 1453. These detections are not physically associated ($0.1 \lesssim z \lesssim 0.5$) with the main galaxies. In Fig. A1, we show the position of these objects in the FoV of the galaxies, while in Table A1 we summarize their main properties.

3 RESULTS

3.1 Ionized gas structure: $\text{H}\alpha$ and $[\text{N II}] \lambda 6584$ emission-line maps and extinction correction

3.1.1 Emission-line morphology

To assist understanding of the physical conditions and detection of the extended and diffuse line-emitting gas, we created continuum-subtracted $\text{H}\alpha + [\text{N II}] \lambda \lambda 6548, 6584$ ($\text{H}\alpha + [\text{N II}]$) emission-line images by subtracting the continuum SED models, as explained in Section 2.2, and then summing the flux in the data cubes between

6528 and 6604 Å. In Figs 3 and B1 (Appendix B available as supplementary online material) we show the maps resulting from this procedure for each galaxy. We also show, in these figures, the continuum-subtracted MUSE spectra from the nuclear 3 arcsec aperture covering the wavelength range from 6400 to 6800 Å as an inset panel within each image. The DIG and extended filamentary line-emitting $\text{H}\alpha + [\text{N II}]$ gas reaches values of $\sim 10^{-19}$ (e.g. NGC 4008) to $\sim 10^{-17}$ (e.g. NGC 5846) $\text{erg cm}^{-2} \text{s}^{-1}$ per pixel.

We used the continuum-subtracted $\text{H}\alpha + [\text{N II}]$ images to classify the galaxies in our sample. To identify the morphology of the line-emitting regions and determine how much these lines correlate with the overall morphology and properties of our sample galaxies, we divided the galaxies into three morphological groups or types: *type i0* – strong or diffuse nuclear emission (i.e. within a ~ 1.5 arcsec radius from the galaxy centre) with (or without) unextended ($\lesssim 1$ kpc) filamentary structures connected to the nuclear region, *type i* – strong or diffuse nuclear emission with extended (several kpc) filamentary structures beyond the nuclear region, and *type ii* – *i0* or *i* plus extranuclear H II regions (well-defined or in distorted ring-like structures). Using this simple classification scheme we find that 7/18 (NGC 410, NGC 777, NGC 978, NGC 4008, NGC 4261, NGC 6658, and NGC 7619) are type *i0*, another 7/18 are type *i* (NGC 193, NGC 584, NGC 677, NGC 1060, NGC 1453, NGC 1587, and NGC 5846), and 4/18 galaxies are type *ii* (NGC 924, NGC 940, NGC 4169, and ESO0507-G025).

3.1.2 Intrinsic reddening

We computed the extinction corrections with the colour excess $E(B - V)$ from the gas using the Balmer decrement $\text{H}\alpha/\text{H}\beta = 2.86$ assuming case B recombination (Osterbrock & Ferland 2006, $n_e = 100 \text{ cm}^{-3}$ and $T_e = 10^4 \text{ K}$). The $E(B - V)_{\text{gas}}$ is calculated as follows:

$$E(B - V)_{\text{gas}} = \frac{2.5}{\kappa(\text{H}\beta) - \kappa(\text{H}\alpha)} \log \left(\frac{(\text{H}\alpha/\text{H}\beta)_o}{2.86} \right), \quad (1)$$

where $\kappa(\text{H}\alpha)$ and $\kappa(\text{H}\beta)$ are the extinction values from the Cardelli et al. (1989) curve with $R_V = 3.1$. $(\text{H}\alpha/\text{H}\beta)_o$ is the observed ratio between $\text{H}\alpha$ and $\text{H}\beta$. Therefore, we corrected the emission lines for extinction using $I_\lambda = F_{\lambda, o} 10^{0.4E(B-V)_{\text{gas}}\kappa(\lambda)}$. The reddening parameters were set to 0.0 for unrealistic values of $(\text{H}\alpha/\text{H}\beta)_o < 2.86$ and when $\text{H}\beta$ was not detected. The assumption of $(\text{H}\alpha/\text{H}\beta)_o = 2.86$ instead of 3.1 in spectra with AGN(-like) features does not significantly affect the results. Galaxies with $(\text{H}\alpha/\text{H}\beta)_o > 2.86$ have low-reddening $E(B - V)_{\text{gas}}$ values from 0.13 to 0.46 mag. This result is not surprising as low Balmer decrements are also found in other ETGs (e.g. Annibali et al. 2010) and in the nuclei and nebular filaments of cool-core clusters (McDonald et al. 2012). On the other hand, ~ 72 per cent (13/18) and ~ 83 per cent (15/18) of our galaxies have unrealistic nuclear and integrated $(\text{H}\alpha/\text{H}\beta)_o$ values, respectively. This indicates that the derived $\text{H}\beta$ fluxes are larger for their corresponding $\text{H}\alpha$ fluxes. For galaxies with $(\text{H}\alpha/\text{H}\beta)_o > 2.86$ the $E(B - V)_{\text{nebular}}$ are similar or slightly lower than the $E(B - V)_{\text{stellar}}$, while for galaxies with $(\text{H}\alpha/\text{H}\beta)_o < 2.86$ the $E(B - V)_{\text{stellar}}$ is higher. This might produce an under subtraction of the observed stellar populations. It is worth noting that unrealistic extinctions are also obtained with other SSP codes (e.g. Annibali et al. 2010; Herpich et al. 2018) in ETGs. However, uncertainties in the reddening correction produced by the stellar fitting will not significantly affect the emission-line ratios or the properties obtained from them in our case. Therefore, large errors in the $\text{H}\alpha/\text{H}\beta$ are due to the uncertainty in the $\text{H}\beta$ emission.

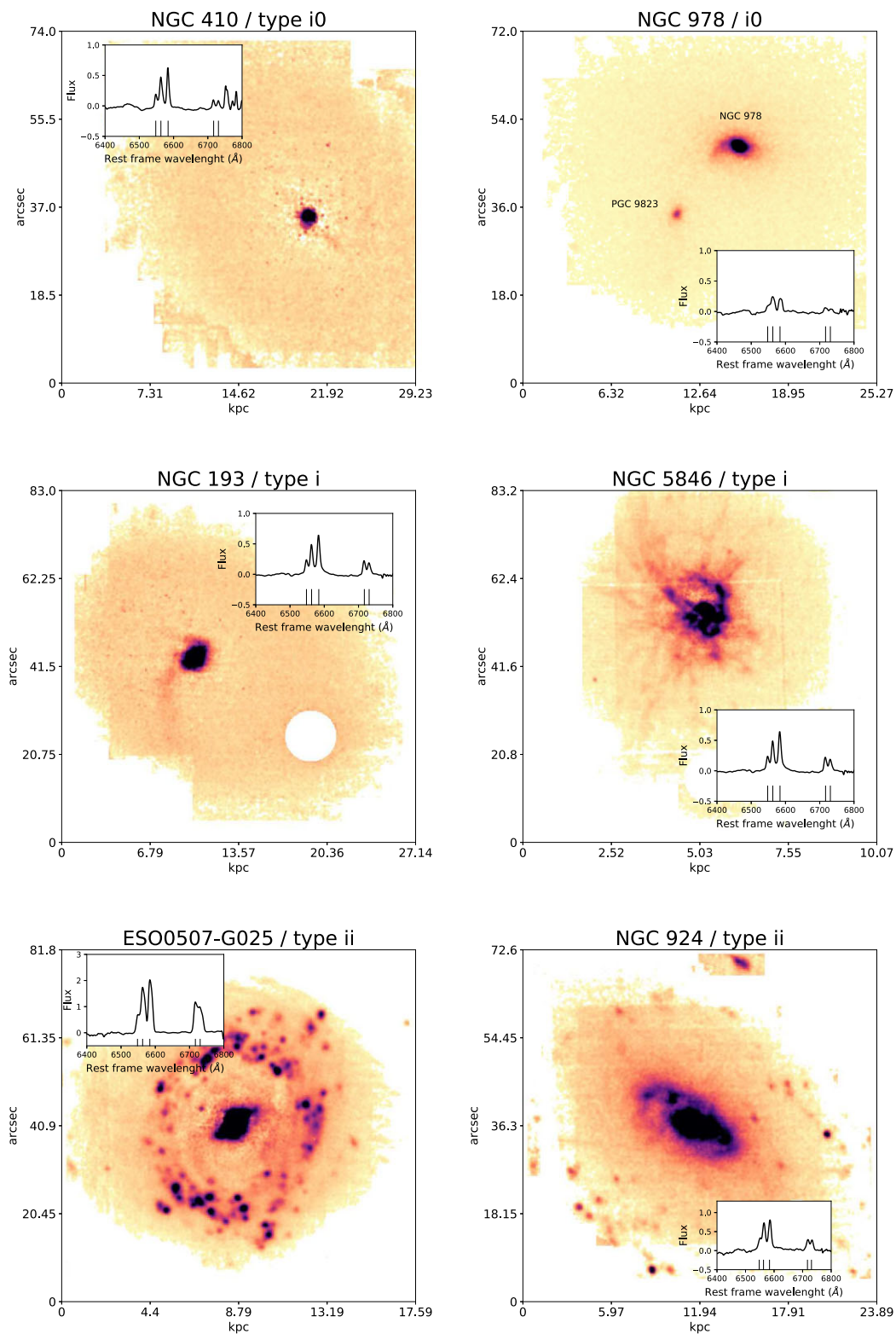


Figure 3. Example of $H\alpha + [N II] \lambda\lambda 6548, 6584$ emission-line maps from our sample. We smoothed the emission-line maps using a 3×3 box filter. MUSE continuum-subtracted spectra from a nuclear 3 arcsec aperture covering the wavelength range from 6400 to 6800 Å are shown in the inset panels. The vertical lines in the inset panels indicate the wavelengths of the [N II] $\lambda 6548$, H α , [N II] $\lambda 6584$, [S II] $\lambda 6717$, and [S II] $\lambda 6731$ emission lines. Fluxes are in units of $\times 10^{-15}$ ($\text{erg s}^{-1} \text{cm}^{-2} \text{\AA}^{-1}$). In Appendix B, available as supplementary online material, we show the emission-line maps of all galaxies in our sample. The companion galaxy of NGC 978 is indicated in the figure. North is to the top and East to the left.

Table 2. $H\alpha + [N II]$ morphology, observed emission-line fluxes, and $EW(H\alpha)$ for our sample galaxies from a simulated 3 arcsec diameter and an integrated (int) aperture. The radial size of the integrated aperture is shown in parentheses to the right of $F(H\alpha)$.

	$H\alpha + [N II]$ morphology	$F(H\alpha)$ ($\times 10^{-14}$ erg cm^{-2} s^{-1})		$(F(H\alpha)/F(H\beta)) \times 100$		$F([N II] \lambda 6584)$ ($\times 10^{-14}$ erg cm^{-2} s^{-1})		$EW(H\alpha)$ (\AA)	
		3 arcsec	int	3 arcsec	int	3 arcsec	int	3 arcsec	int
NGC 193	i	0.43 ± 0.02	1.64 ± 0.11 (6.0 arcsec)	245.16 ± 0.31	134.39 ± 0.25	0.59 ± 0.06	1.70 ± 0.22	2.71	1.65
NGC 410	i0	0.52 ± 0.01	0.83 ± 0.02 (4.5 arcsec)	146.81 ± 0.11	112.64 ± 0.14	0.52 ± 0.04	0.87 ± 0.08	1.63	0.69
NGC 584	i	0.66 ± 0.07	5.83 ± 0.67 (21.0 arcsec)	205.26 ± 0.69	131.12 ± 0.88	0.90 ± 0.08	4.1 ± 0.7	0.77	0.53
NGC 677	i	0.63 ± 0.03	4.51 ± 0.45 (7.5 arcsec)	322.66 ± 0.36	313.84 ± 0.60	0.62 ± 0.07	3.87 ± 0.60	3.43	3.13
NGC 777	i0	0.10 ± 0.01	–	25.55 ± 0.09	–	0.19 ± 0.01	–	0.28	–
NGC 924	ii	0.83 ± 0.06	3.83 ± 0.30 (24 arcsec)	257.83 ± 0.66	246.32 ± 1.24	0.96 ± 0.06	3.48 ± 0.25	2.24	1.60
NGC 940	ii	0.52 ± 0.04	10.01 ± 0.24 (13.5 arcsec)	436.02 ± 1.12	287.04 ± 0.31	1.14 ± 0.10	6.49 ± 0.77	2.22	5.06
NGC 978	i0	0.33 ± 0.02	0.81 ± 0.08 (4.5 arcsec)	148.83 ± 0.19	104.83 ± 0.21	0.28 ± 0.02	0.70 ± 0.08	1.23	0.81
NGC 1060	i	0.37 ± 0.05	1.37 ± 0.23 (6.0 arcsec)	202.02 ± 1.96	129.84 ± 0.73	0.46 ± 0.04	1.18 ± 0.19	0.86	0.63
NGC 1453	i	1.35 ± 0.06	8.14 ± 0.79 (13.5 arcsec)	188.92 ± 0.21	91.13 ± 0.19	2.07 ± 0.08	9.43 ± 0.82	2.60	2.00
NGC 1587	i	0.63 ± 0.04	5.14 ± 0.18 (15 arcsec)	227.91 ± 0.40	161.05 ± 0.33	0.75 ± 0.04	4.13 ± 0.22	1.50	1.41
NGC 4008	i0	0.16 ± 0.02	–	–	–	0.14 ± 0.02	–	0.46	–
NGC 4169	ii	0.99 ± 0.05	4.67 ± 0.28 (10.5 arcsec)	325.06 ± 0.57	235.69 ± 0.76	1.71 ± 0.06	6.63 ± 0.36	2.24	1.35
NGC 4261	i0	4.31 ± 0.58	–	450.88 ± 0.78	–	9.44 ± 0.64	–	2.61	–
ESO0507-G025	ii	2.59 ± 0.14	20.37 ± 1.34 (27.0 arcsec)	363.09 ± 0.32	291.93 ± 0.29	2.9 ± 0.18	13.68 ± 1.95	5.93	3.65
NGC 5846	i	0.74 ± 0.07	11.33 ± 1.27 (18 arcsec)	189.27 ± 0.35	139.11 ± 0.30	0.98 ± 0.09	11.46 ± 1.44	2.10	1.49
NGC 6658	i0	0.15 ± 0.02	–	242.79 ± 1.89	–	0.23 ± 0.02	–	0.47	–
NGC 7619	i0	0.19 ± 0.05	–	36.63 ± 0.13	–	0.47 ± 0.04	–	0.31	–

3.2 $[O III] \lambda 5007/H\beta$, $[S II] \lambda \lambda 6717, 6731/H\alpha$, and $[N II] \lambda 6584/H\alpha$ emission-line ratio maps and BPT diagrams

Using the information derived in the previous sections it is possible to distinguish between different ionization mechanisms using BPT (Baldwin, Phillips & Terlevich 1981) diagrams. To do this, we used the following emission-line ratios: $[O III] \lambda 5007/H\beta$ ($[O III]/H\beta$) and $[N II] \lambda 6584/H\alpha$ ($[N II]/H\alpha$). The $[O III] \lambda 5007/H\beta$ emission-line ratio is an excitation indicator and provides information about the available fraction of hard ionizing photons. On the other hand, $[N II] \lambda 6584$ is a low-ionization emission-line tracer, which is usually weak in pure $H II$ regions. Therefore, the emission-line ratios $[N II]/H\alpha$ and $[O III]/H\beta$ can effectively discriminate between photoionization under physical conditions that are typical for $H II$ regions and other excitation mechanisms (e.g. AGN or shocks) which are likely present in our sample. In Fig. 4, we show an example of the emission-line ratio maps $\log([N II]/H\alpha)$ and $\log([O III]/H\beta)$, the $\log([N II]/H\alpha)$ versus $\log([O III]/H\beta)$ BPT diagram, and the 2D BPT map for the galaxy ESO0507-G025. In this figure, we separate star-forming and AGN-ionized regions (i.e. Seyferts and LINERs) with blue demarcation lines from models by Kauffmann et al. (2003) (dotted line), Kewley et al. (2001) (solid line), and Schawinski et al. (2007) (dashed line). We colour-coded the data points located in the different areas of the BPT diagram, i.e. AGN/LINERs in red, composite in orange, and the star-forming $H II$ -dominated area in green. In Appendix C, available as supplementary online material, we show the emission-line ratio maps and the BPT diagrams/maps for our entire sample. The BPT maps show that most of our data points/spaxels in the nuclear regions (see Fig. 4) are dominated by AGN/LINERs, while the SF becomes more important in the extended regions. We note that, in most cases, we obtain a very small or non-existent number of data points (~ 17 per cent of the spaxels in ESO0507-G025) in the $H II$ area of the BPT diagrams (see figures in Appendix C). Most spaxels lie in the AGN/LINERs region of the diagrams (~ 71 per cent of the spaxels on average), while only in two cases (NGC 978 and ESO0507-G025) are most spaxels in the composite region with 62 per cent and 55 per cent of the spaxels, respectively.

In Table 3, we present for each galaxy the emission-line ratios $\log([O III]/H\beta)$, $\log([N II]/H\alpha)$, and $\log([S II]/H\alpha)$ from the 3

arcsec and integrated apertures. Fig. 5 shows the BPT diagram $[O III]/H\beta$ versus $[N II]/H\alpha$ of the nuclear regions (small squares) for galaxies where $[O III] \lambda 5007$ and $H\beta$ are detected. In the figure, we compare these with values obtained from the integrated apertures (circles). We use the same colour code to identify the galaxies in this diagram throughout the paper. In most cases, the nuclear values lie in the LINER region of the BPT diagram, while the integrated ones are in the composite region. The $\log([O III]/H\beta)$ for most galaxies decreases significantly when we consider the larger integrated aperture, which changes their positions in the BPT diagram. In the case of ESO0507-G025, NGC 924, and NGC 5846 the $\log([O III]/H\beta)$ increases and the $\log([N II]/H\alpha)$ ratio decreases. Fig. 5 clearly shows that the ionization structure of our sample galaxies cannot be correctly assessed from small fixed apertures (e.g. SDSS aperture) and the ionization sources and structure of the warm gas may be different in different parts of the galaxies (see Appendix C). In Sections 4.1 and 4.2, we explore the effect of using different apertures on the observed properties of the ISM and the ionization mechanisms likely present in our sample galaxies.

In summary, we find that all galaxies in our sample, with $[O III] \lambda 5007$ and $H\beta$ detections, have a dominant AGN/LINER nuclear region. Extended LINER-like regions are observed in most galaxies with filamentary structures (type i galaxies) and ring-like structures and/or extranuclear $H II$ regions (type ii galaxies). Most spaxels in these regions fall in the BPT area of mixed contribution (composite) from SF and/or AGNs.

3.3 Velocity field maps

We obtained the radial velocity $V([N II])$ and velocity dispersion $\sigma([N II])$ maps by fitting a single Gaussian to the $[N II] \lambda 6584$ emission-line profiles. The velocity dispersion σ (or $FWHM = 2.35\sigma$) was obtained as $\sigma^2 = \sigma_{obs}^2 - \sigma_{inst}^2$, where σ_{inst} is the instrumental dispersion, see Section 2.1. The detailed kinematical analysis of the emitting gas is beyond the scope of this paper; however, in Fig. 6 and Appendix D (supplementary online material) we show the velocity field maps for the type ii galaxies ESO0507-G025 and NGC 924, NGC 940, and NGC 4169, respectively. Radial

ESO0507-G025

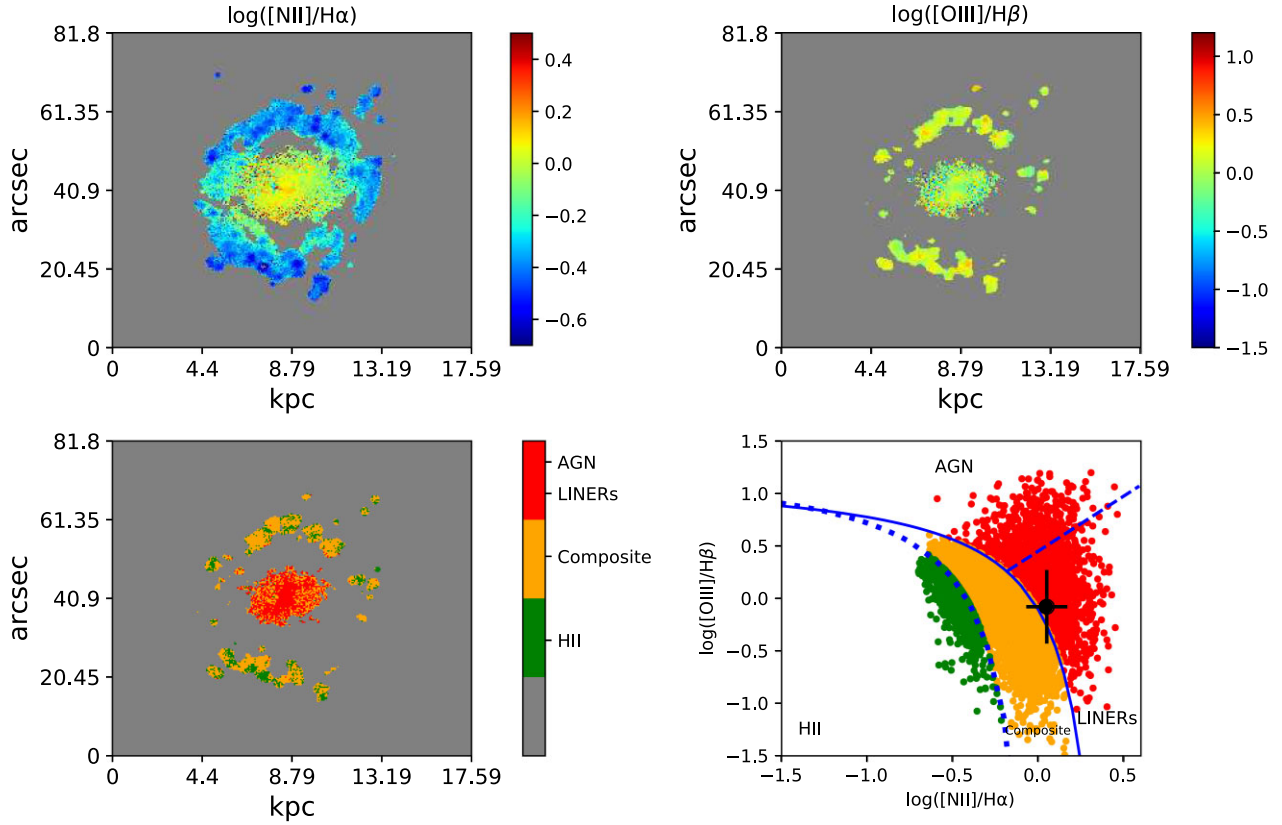


Figure 4. Example of our emission-line ratio maps $\log([\text{N II}]/\text{H}\alpha)$ and $\log([\text{O III}]/\text{H}\beta)$ (top row), and BPT diagrams (bottom row) for the galaxy ESO0507-G025. In the BPT diagrams we include the Kewley et al. (2001; solid line), Kauffmann et al. (2003; dotted line), and Schawinski et al. (2007; dashed line) model boundary lines which divide regions dominated by star-forming H II (green), composite (orange data points), and AGN/LINERs (red data points). The filled black data point corresponds to value in the 3 arcsec aperture. In Appendix C, available as supplementary online material, we show the emission-line ratio maps and the BPT diagrams/maps for our entire sample. North is to the top and East to the left.

Table 3. Main properties of our sample galaxies from the simulated SDSS spectral fibre diameter (3 arcsec) and integrated (int) apertures. $\text{SFR}(\text{H}\alpha)$ calculated from the $L(\text{H}\alpha)$ in the largest aperture int/3 arcsec.

	$\log([\text{O III}]/\text{H}\beta)$		$\log([\text{N II}]/\text{H}\alpha)$		$\log([\text{S II}]/\text{H}\alpha)$		$L(\text{H}\alpha)$ ($\times 10^{39} \text{ erg cm}^{-1}$)		$\text{SFR}(\text{H}\alpha)$ ($M_{\odot} \text{ yr}^{-1}$)
	3 arcsec	int	3 arcsec	int	3 arcsec	int	3 arcsec	int	
NGC 193	-0.27 ± 0.22	-0.49 ± 0.40	0.14 ± 0.16	0.02 ± 0.20	-0.02 ± 0.15	-0.14 ± 0.22	2.01 ± 0.12	7.70 ± 0.52	0.0354 ± 0.0024
NGC 410	–	–	0.01 ± 0.11	0.02 ± 0.12	-0.33 ± 0.15	-0.13 ± 0.17	3.55 ± 0.08	5.72 ± 0.13	0.0263 ± 0.0006
NGC 584	-0.04 ± 0.40	-0.17 ± 1.03	0.13 ± 0.19	-0.15 ± 0.29	-0.16 ± 0.34	-0.44 ± 0.75	0.53 ± 0.06	4.68 ± 0.54	0.0215 ± 0.0025
NGC 677	-0.06 ± 0.22	-0.15 ± 0.30	-0.01 ± 0.16	-0.07 ± 0.23	-0.03 ± 0.08	-0.09 ± 0.15	5.22 ± 0.24	34.71 ± 3.50	0.1597 ± 0.0161
NGC 777	–	–	0.28 ± 0.22	–	0.30 ± 0.28	–	0.61 ± 0.09	–	0.0028 ± 0.0004
NGC 924	0.05 ± 0.37	0.14 ± 0.60	0.06 ± 0.14	-0.04 ± 0.15	-0.10 ± 0.20	-0.12 ± 0.27	3.97 ± 0.28	18.24 ± 1.41	0.0839 ± 0.0065
NGC 940	0.19 ± 0.43	-0.55 ± 0.36	0.34 ± 0.17	-0.19 ± 0.14	0.02 ± 0.25	-0.45 ± 0.20	8.84 ± 0.75	63.67 ± 1.50	0.2929 ± 0.0069
NGC 978	-0.09 ± 0.17	-0.15 ± 0.22	-0.08 ± 0.14	-0.07 ± 0.22	-0.18 ± 0.21	-0.11 ± 0.42	1.81 ± 0.21	4.40 ± 0.49	0.0203 ± 0.0023
NGC 1060	–	–	0.10 ± 0.23	-0.06 ± 0.33	0.09 ± 0.44	0.18 ± 0.57	2.38 ± 0.33	8.80 ± 1.51	0.0405 ± 0.0069
NGC 1453	-0.27 ± 0.26	-0.52 ± 0.37	0.19 ± 0.08	0.06 ± 0.18	0.09 ± 0.08	-0.12 ± 0.17	4.52 ± 0.19	27.23 ± 2.64	0.1253 ± 0.0121
NGC 1587	0.27 ± 0.16	-0.05 ± 0.34	0.07 ± 0.11	-0.09 ± 0.09	0.03 ± 0.16	-0.11 ± 0.23	1.88 ± 0.11	15.37 ± 0.52	0.0707 ± 0.0024
NGC 4008	–	–	-0.07 ± 0.25	–	0.09 ± 0.41	–	0.47 ± 0.06	–	0.0022 ± 0.0003
NGC 4169	-0.05 ± 0.32	-0.16 ± 0.51	0.24 ± 0.08	0.15 ± 0.12	0.10 ± 0.16	0.10 ± 0.15	4.24 ± 0.19	14.75 ± 0.90	0.0679 ± 0.0041
NGC 4261	0.25 ± 0.48	–	0.34 ± 0.20	–	-0.07 ± 0.29	–	12.08 ± 1.62	–	0.0556 ± 0.0074
ESO0507-G025	-0.08 ± 0.35	0.02 ± 0.34	0.05 ± 0.12	-0.17 ± 0.21	0.07 ± 0.15	-0.16 ± 0.26	9.17 ± 0.52	42.56 ± 2.96	0.1958 ± 0.0136
NGC 5846	-0.40 ± 0.19	-0.24 ± 0.41	0.12 ± 0.18	0.01 ± 0.24	-0.12 ± 0.21	-0.26 ± 0.43	0.47 ± 0.04	7.23 ± 0.81	0.0333 ± 0.0037
NGC 6658	0.54 ± 0.79	–	0.19 ± 0.19	–	–	–	0.65 ± 0.08	–	0.0030 ± 0.0004
NGC 7619	–	–	0.40 ± 0.36	–	–	–	0.66 ± 0.17	–	0.0030 ± 0.0008

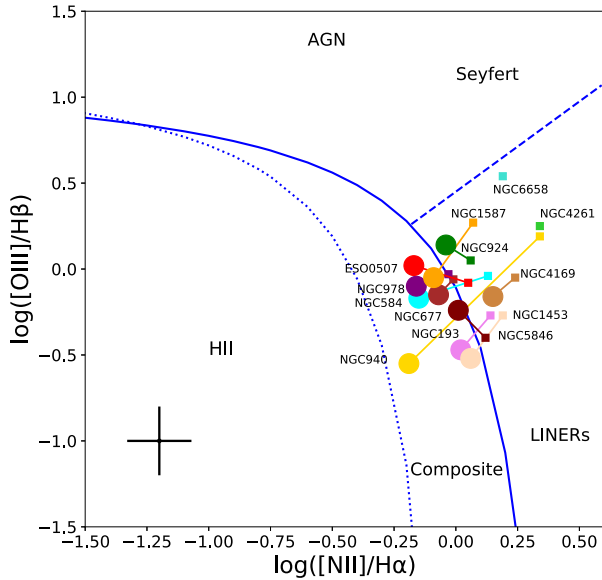


Figure 5. $[\text{O III}]/\text{H}\beta$ versus $[\text{N II}]/\text{H}\alpha$ diagnostic diagram for the nuclear spectra using equivalent 3 arcsec apertures to SDSS spectra (squares) and integrated emission (circles). The Kewley et al. (2001; solid line), Kauffmann et al. (2003; dotted line), and Schawinski et al. (2007; dashed line) model boundary lines in blue discriminate between areas of the diagram dominated by SF (H II) and AGNs/LINERs emission. The mean errors are shown in the lower of the figure.

velocity and velocity dispersion maps for our full sample are shown in Olivares et al. (2022). In order to include the kinematical information from the extended and filamentary structures, we considered spaxels with $\text{S/N} \gtrsim 2$. In Fig. 6, we see an example of these velocity fields for the galaxy ESO0507-G025. Clearly, this galaxy has two independent velocity structures or rotating discs, while the velocity dispersion in the nuclear region shows a bicone-shaped structure which increases in velocity dispersion with distance from the centre. The gas in these bicone structures is located in the AGNs/LINERs region of the BPT diagram (see Figs 4 and 5), suggesting an outflow perpendicular to the observer.

Our velocity fields (V and σ) are in agreement with those obtained independently by Olivares et al. (2022). In general, the radial velocity fields in our sample galaxies (see Appendix D and Olivares et al. 2022) show rotation or gradients but with relatively small velocity ranges of around $\pm 200\text{--}300 \text{ km s}^{-1}$. These variations are similar in both, the compact and extended gas emission regions. We see the highest $\sigma([\text{N II}])$ values, in most cases, at positions close to the continuum flux maximum with values of ~ 150 to $\sim 300 \text{ km s}^{-1}$, while extended regions or filaments show lower values. In general $\sigma([\text{N II}])$ values in the filaments vary little across the galaxies. This trend was also reported by McDonald et al. (2012) for a sample of galaxies in galaxy clusters. They found that the most extended optical filaments in their sample, likely originated from ICM cooling and were experiencing only minor turbulence.

3.4 $[\text{S II}]\lambda 6716/[\text{S II}]\lambda 6731$ ratio

The $[\text{S II}]\lambda 6716/[\text{S II}]\lambda 6731$ intensity ratio was used to determine the electron density $n_e([\text{S II}])$. We computed the values of $n_e([\text{S II}])$ using the IRAF STS temden package assuming $t_e([\text{O III}]) = 10\,000 \text{ K}$. We set unrealistic (saturated) values of $[\text{S II}]\lambda 6716/[\text{S II}]\lambda 6731 > 1.43$ to $n_e([\text{S II}]) \sim 1 \text{ cm}^{-3}$ and for $[\text{S II}]\lambda 6716 / [\text{S II}]\lambda 6731 < 0.46$ to

$\sim 52\,452 \text{ cm}^{-3}$. In Table 4, we show the electron density for the nuclear (3 arcsec aperture) regions for our sample. We note that the $[\text{S II}]\lambda 6716/[\text{S II}]\lambda 6731$ ratio is greater than 1 for 12/18 galaxies, which indicates a predominantly low-density regime ($\sim 100 \text{ cm}^{-3}$). Only 6/18 galaxies show values $\gtrsim 1000 \text{ cm}^{-3}$ in the nuclear regions. In Fig. E1 (Appendix E available as supplementary online material) we show the $[\text{S II}]\lambda 6716 / [\text{S II}]\lambda 6731$ ratio maps for our sample galaxies.

Interestingly, the ionization cones observed in ESO0507-G025 (see the emission-line ratio maps $[\text{O III}]/\text{H}\beta$ and $[\text{N II}]/\text{H}\alpha$ in Fig. 4 and velocity fields in Fig. 6) together with the high electron density and the shape of the spatially resolved $[\text{S II}]\lambda 6716/[\text{S II}]\lambda 6731$ ratio map indicate that the central region of this galaxy is almost certainly ionized by an AGN (e.g. Kakkad et al. 2018). This clear pattern is not observed in our other galaxies. In general, the presence of high electron density in the nuclear regions and extended enhanced regions with densities $\gtrsim 1000 \text{ cm}^{-3}$ could indicate outflowing ISM likely driven by expanding hot gas heated by SNe, SF stellar winds, AGN activity, and/or the collision/interaction of galaxies (Westmoquette et al. 2012). We will discuss in detail in Section 4 the results obtained in this section and their implications for the evolutionary stages of the gas in our sample galaxies.

3.5 Star formation rate

Following a common practice, the current star formation rates (SFRs) were estimated from the integrated $\text{H}\alpha$ luminosity $L(\text{H}\alpha)$, assuming the Kennicutt (1998) formula, for a solar metallicity, after correction for a Chabrier (2003) IMF, i.e. $\text{SFR}(\text{H}\alpha) (M_{\odot} \text{ yr}^{-1}) = 4.6 \times 10^{-42} \times L(\text{H}\alpha) (\text{erg s}^{-1})$ (Parkash et al. 2019). However, it is unlikely in our case that all $\text{H}\alpha$ emission results from SF, since the BPT diagnostics indicate a LINER or composite nature for most spaxels in our emission-line maps. Therefore, the derived SFRs are likely to be an overestimate and are included here for comparison with other studies. Table 3 shows the resultant SFRs, obtained from the integrated apertures of the galaxies.

We note that, our average, SFRs are ~ 16 per cent lower than that found by Kolokythas et al. (2022) using *GALEX* FUV fluxes as SF indicator, while FIR SFRs (O’Sullivan et al. 2015) for some of our galaxies (NGC 777, NGC 940, NGC 1060, and NGC 5846) are one or two orders of magnitude higher than our $\text{SFR}(\text{H}\alpha)$. Contamination of the FIR luminosity as an SF tracer cannot be discarded. Most galaxies in both samples are AGN-dominated at FIR wavelengths and their derived FIR SFRs are greater than that expected from SF. However, in the case of NGC 940, they do not confirm the presence of a radio AGN (O’Sullivan et al. 2015). In summary, we find that in this and the aforementioned studies, the SFRs in type i and type ii group-dominant galaxies, on average, are higher than those in type i0 galaxies.

4 DISCUSSION

4.1 Aperture effects

As shown in Section 3.2, aperture selection and 2D mapping can impact conclusions about the dominant mechanism ionizing the gas in our sample. This was demonstrated in Fig. 5 where we show the $[\text{O III}]/\text{H}\beta$ versus $[\text{N II}]/\text{H}\alpha$ diagnostic diagram for the nuclear and integrated apertures. The displacement of the data points in this diagram when the aperture is increased indicates how our interpretation about the ionizing sources can change depending on aperture size. The limitations of using SDSS spectra for nearby

Table 4. Electron density for the nuclear (3 arcsec aperture) regions of our sample of group-dominant galaxies. We show the unrealistic (saturated) values of $[\text{S II}] \lambda 6716 / [\text{S II}] \lambda 6731$ by ✓ symbols.

Name	$[\text{S II}] \lambda 6716 / [\text{S II}] \lambda 6731$	Saturated values	$n_e([\text{S II}])$ (cm^{-3})
NGC 193	0.92 ± 0.16		839.3 ± 397.4
NGC 410	1.85 ± 0.23	✓	≤ 1.0
NGC 584	1.46 ± 0.70	✓	≤ 1.0
NGC 677	1.29 ± 0.09		131.3 ± 98.0
NGC 777	1.11 ± 0.30		377.5 ± 653.8
NGC 924	1.38 ± 0.36		43.7 ± 257.3
NGC 940	1.06 ± 0.34		471.4 ± 992.9
NGC 978	1.23 ± 0.37		200.8 ± 436.0
NGC 1060	0.66 ± 0.37		2788.0 ± 1126.3
NGC 1453	1.29 ± 0.10		131.3 ± 109.2
NGC 1587	1.21 ± 0.24		226.4 ± 229.5
NGC 4008	0.69 ± 0.39		2352.9 ± 960.4
NGC 4169	1.07 ± 0.25		451.4 ± 584.7
NGC 4261	1.12 ± 0.36		360.4 ± 649.3
ESO0507-G025	0.46 ± 0.09		$48\,893.1 \pm 21\,200.4$
NGC 5846	1.06 ± 0.24		471.4 ± 574.6
NGC 6658	0.29 ± 0.12	✓	$\gtrsim 52\,452.0$
NGC 7619	0.74 ± 0.11		1823.7 ± 1122.5

galaxies has also been highlighted recently using IFU spectroscopy (see Gomes et al. 2016, and references therein). In our case, we can see that in the innermost part of the galaxies, the gas is likely dominated by shocks and/or AGN activity given that the nuclear gas emission-line ratios lie in the LINER region of the BPT diagram; however, at large apertures photoionization by OB stars likely becomes increasingly more important.

In Fig. 7, we show the effects of using different apertures on the observed properties of our sample. In panel (a) we show the $L(\text{H}\alpha)$ surface density $\Sigma(\text{H}\alpha)$ calculated as $L(\text{H}\alpha)/\text{area}$, in (b) the $\text{EW}(\text{H}\alpha)$, and panel (c) shows the $\log([\text{N II}]/\text{H}\alpha)$ emission-line ratio. In this figure, the apertures were selected to increase in steps of 1.5 arcsec of radius. The Σ , in panel (a) of Fig. 7, in all cases decreases with radius and shows the presence of extended $\text{H}\alpha$ emission beyond the

SDSS aperture. Cid Fernandes et al. (2011) used the $\text{EW}(\text{H}\alpha)$ as an alternative method (explained below in Section 4.2) to the BPT diagrams (emission-line classification). Using this method, Gomes et al. (2016) argue that evolved pAGB stellar background is sufficient to photoionize the diffuse gas in ETGs and explain the observed $\text{EW}(\text{H}\alpha)$ in the range $0.5\text{--}2.4 \text{ \AA}$. Most $\text{EW}(\text{H}\alpha)$ values in panel (b), irrespective of aperture, lie within the area (grey region in the panel) which is consistent with pure pAGB photoionization (Cid Fernandes et al. 2011; Gomes et al. 2016). We find that one type ii galaxy (ESO0507-G025) and three type i galaxies (NGC 193, NGC 677, and NGC 1453) show $\text{EW}(\text{H}\alpha) > 2.4 \text{ \AA}$ at their centres. These results indicate that pAGBs alone do not explain the observed values in these regions. The $\text{EW}(\text{H}\alpha)$ values of remaining galaxies are consistent with pure pAGB emission. The $[\text{N II}]/\text{H}\alpha$ found in the nuclear regions (SDSS aperture; see panel c) and at large radii, in most cases, is consistent with LINER emission since $\log([\text{N II}]/\text{H}\alpha) \gtrsim 0.0$. We observe that the $\log([\text{N II}]/\text{H}\alpha)$ declines with increasing apertures in almost all cases, although the radial profiles differ significantly.

4.2 Ionization mechanisms

In this section, we examine the mechanisms responsible for the ionization which produces the optical emission lines in our sample. For this, we use photoionization models from the literature, which incorporate the expected physical conditions in our sample galaxies.

In Fig. 8, we show the BPT diagram for the nuclear emission for our sample galaxies. The fill colour of the data points indicates the $\text{EW}(\text{H}\alpha)$ from the colour scale and the edge colour of the circles identifies the galaxies from the legend. Superimposed on the plot are shock models from Allen et al. (2008) calculated with the MAPPINGS III shock and photoionization code. These shock models have solar metallicity, densities from $n = 0.01$ to 1000 cm^{-3} , velocities from $v = 100$ to 1000 km s^{-1} , and magnetic field $B = 1 \mu\text{G}$. The models for $v = 100 \text{ km s}^{-1}$ (purple), 200 km s^{-1} (red), 300 km s^{-1} (green), 500 km s^{-1} (orange), and 1000 km s^{-1} (blue) are shown as coloured lines. The nuclear regions in our sample lie in the

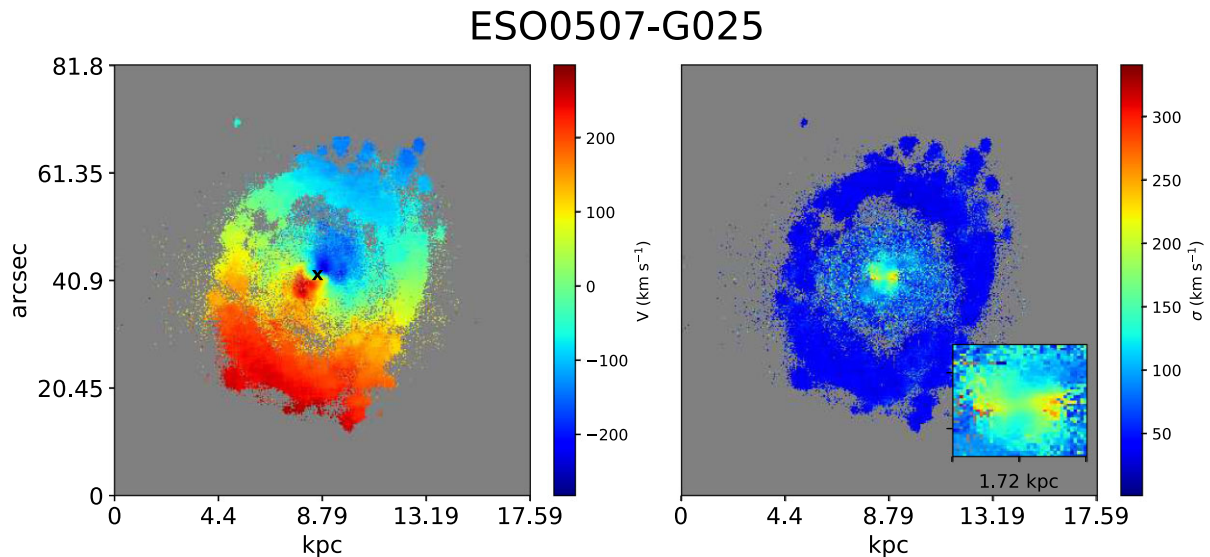


Figure 6. Radial velocity $V([\text{N II}])$ (left-hand panel) and velocity dispersion $\sigma([\text{N II}])$ (right-hand panel) maps for the galaxy ESO0507-G025. The position of the continuum maximum is indicated by an X symbol. A zoom-in of the central region of the velocity dispersion map is shown in the inset panel. In appendix D, available as supplementary online material, we show the velocity field maps for the type ii galaxies NGC 924, NGC 940, and NGC 4169, respectively. North is up and east is to the left.

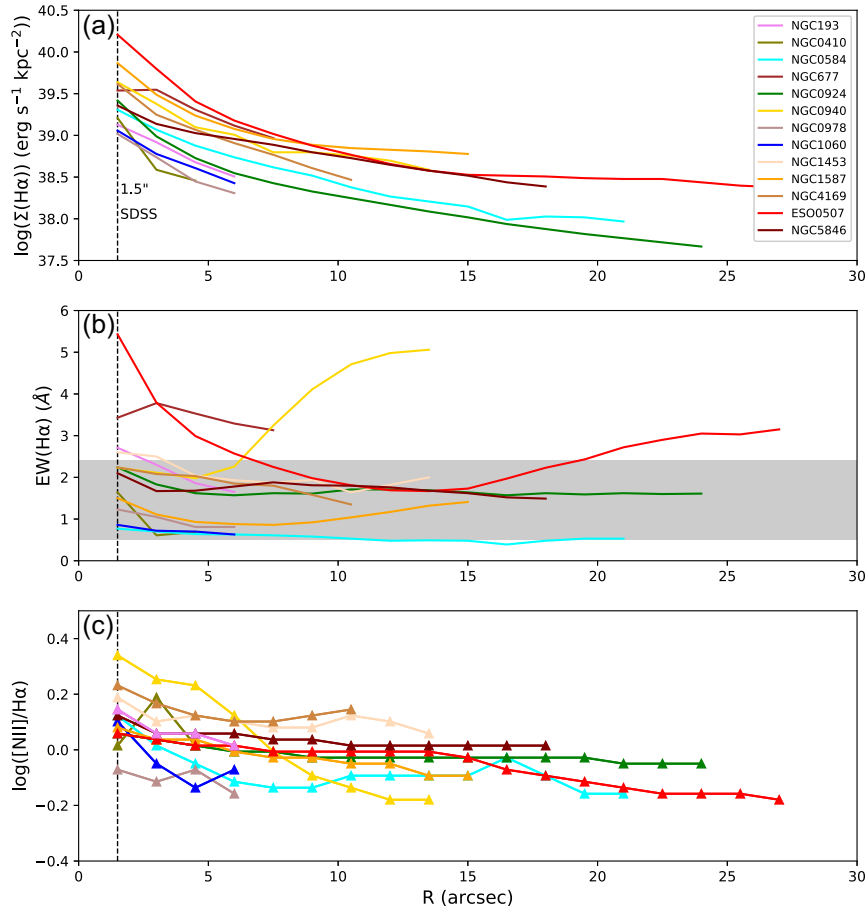


Figure 7. Observed gas properties as a function of 1.5 arcsec aperture bins. (a) Luminosity surface density $\Sigma(\text{H}\alpha)$. (b) $\text{EW}(\text{H}\alpha)$, the grey region between 0.5 and 2.4 Å is consistent with pure pAGB photoionization. For points with $\text{EW}(\text{H}\alpha) > 2.4$ Å an additional gas excitation source is needed to account for the observed $\text{EW}(\text{H}\alpha)$ (Gomes et al. 2016). (c) $\log([\text{NII}]/\text{H}\alpha)$ emission-line ratio. The vertical dotted line indicates the SDSS radial spectra fibre aperture.

velocity range of >200 to $\gtrsim 1000$ km s $^{-1}$ and density between ~ 0.1 and < 100 cm $^{-3}$. Annibali et al. (2010) compared the [S II] densities obtained for a sample of ETGs/LINERs with ionized gas with the Allen et al. (2008) models. The majority of their galaxies had $n_e \gtrsim 100$ cm $^{-3}$ for an assumed $T = 10\,000$ K. But as in our case (see Table 4), a significant fraction of galaxies have saturated [S II] ratios around 1.45 which are consistent with pre-shock densities ($n_e \approx 0.01$ to $\lesssim 100$ cm $^{-3}$). These pre-shock regions are observed in some galaxies of Fig. E1 (appendix E). This could indicate together with the increasing [S II] $\lambda 6716/[\text{S II}] \lambda 6731$ ratios that AGN/SF-driven shocks are ionizing the gas mainly in the nuclear regions. This would be consistent with the Molina et al. (2018) conclusion that the line emission of LINERs with low-luminosity AGNs are predominantly powered by shocked gas due to jets or outflows (see also Edwards et al. 2007).

In Fig. 9 (upper panels), we show the BPT diagrams, as in Fig. 8, but including two different photoionization model grids from Krabbe et al. (2021). Their models consider the main (LINER) properties observed in our sample of group-dominant galaxies for two distinct SEDs. One model assumes pAGB stars (upper left panel) with different T_{eff} as the ionizing source and the other considers AGN SED with a multicomponent continuum (upper right panel). The models were created using the CLOUDY code version 17.0 (Ferland 2017) for metallicities $Z/Z_{\odot} = 0.2, 0.5, 0.75, 1.0, 2.0,$ and 3.0 and ionization parameters U^2 in the range of $-4.0 \leq \log(U) \leq -0.5$ in

steps of 0.5 dex. Their assumed density of $n_e 500$ cm $^{-3}$ is typical for BCGs (e.g. Ciocan et al. 2021) and it is compatible with our values from Section 3.4. In both cases, most galaxies in our sample lie in the region between $Z/Z_{\odot} = 0.75$ ($12 + \log(\text{O}/\text{H}) = 8.56$) and $Z/Z_{\odot} = 1$ ($12 + \log(\text{O}/\text{H}) = 8.69$). However, NGG 4261 and NGC 940 have values compatible with models at $2\text{--}3 Z_{\odot}$ ($12 + \log(\text{O}/\text{H}) = 8.99 - 9.17$), assuming AGN activity. While for pAGB models, the values for NGG 4261, NGC 940, NGC 4169, and NGC 6658 are compatible with models at $> 1.0 Z_{\odot}$ metallicities. These results indicate that the nuclear regions in our sample are consistent, within the uncertainties, with metallicities slightly (above) solar, independent of the ionizing sources. In Section 4.3, we estimate the gas-phase metallicity for each nuclear region in our sample.

In Fig. 9 (bottom panel), we show the BPT diagram overlaid with the predicted emission-line ratios from CLOUDY models obtained by Polles et al. (2021), which include photoionization by X-ray emission. We show, in this figure, models for three values of metallicity $Z/Z_{\odot} = 0.3, 0.65,$ and 1 and several values of X-ray emission $\log(G_x)$ from 2.8 to 1.4 in steps of 0.2 dex with the turbulent velocity (produced by e.g. AGN jets, turbulent mixing between the hot and cold phases, and the collisions between filaments) fixed to 10 km s $^{-1}$ (dotted coloured lines and dotted black lines). In the same panel, we added three models for the aforementioned metallicities and turbulence velocities $v_{\text{tue}} = 30, 10, 2,$ and 0 km s $^{-1}$ (solid coloured lines and small dotted black lines). The X-ray radiation field G_x is fixed to 100. In general, these grid of models can reproduce the observed values without an excess in X-ray luminosity, even if

²The ratio of the ionizing photon density to the particle density.

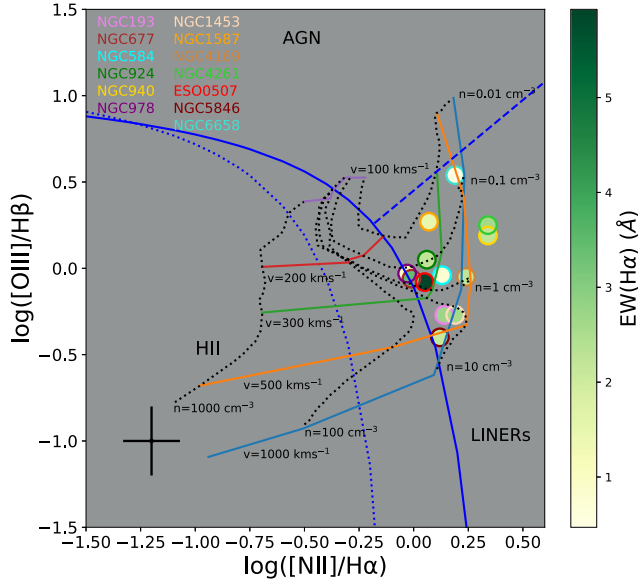


Figure 8. BPT $[\text{O III}]/\text{H}\beta$ versus $[\text{N II}]/\text{H}\alpha$ diagnostic diagram, similar to Fig. 4, for the nuclear spectra (circles). We have superimposed the shock models of Allen et al. (2008) at solar metallicity (more details in the text) and the Kewley et al. (2001; solid line), Kauffmann et al. (2003; dotted line), and Schawinski et al. (2007; dashed line) boundaries as in Fig. 5. The fill colour of the circles indicates the $\text{EW}(\text{H}\alpha)$ and the edge colours identifies the galaxies from the legend.

the optical depth A_V increases (see figs E1 and E2 in Polles et al. 2021). In the case of NGC 5846, the observed emission-line ratios (maroon open circle) are reproduced by models at very low (or no) turbulence velocities. Also, we find no sign of a clear rotational pattern (disturbed velocity field) in the FoV of the galaxy (see the v_r map in Olivares et al. 2022) together with extended filaments of low velocity dispersion. This is in agreement with a cooling flows scenario, where the cool gas may have cooled in (or close to) the centre of the group (Temi et al. 2018; Jung et al. 2022). In addition, in this galaxy there is a good correlation between the CO cloud positions, detected by Temi et al. (2018), and the warm gas emission.

Cid Fernandes et al. (2011) introduced the WHAN diagram which uses the $\text{EW}(\text{H}\alpha)$ (or $W_{\text{H}\alpha}$) in order to discriminate low-ionization AGNs from galaxies that are ionized by evolved pAGB stars. This diagram identifies five classes of galaxies: (1) pure star-forming galaxies: $\log([\text{N II}]/\text{H}\alpha) < -0.4$ and $\text{EW}(\text{H}\alpha) > 3 \text{ \AA}$, (2) strong AGN emission: $\log([\text{N II}]/\text{H}\alpha) > -0.4$ and $\text{EW}(\text{H}\alpha) > 6 \text{ \AA}$, (3) weak AGNs: $\log([\text{N II}]/\text{H}\alpha) > -0.4$ and $\text{EW}(\text{H}\alpha)$ between 3 and 6 \AA , (4) retired galaxies: $\text{EW}(\text{H}\alpha) < 3 \text{ \AA}$, and (5) passive galaxies: $\text{EW}(\text{H}\alpha)$ and $\text{EW}([\text{N II}]) < 0.5 \text{ \AA}$. According to this classification scheme most of our sample (see Fig. 10) can be classified as retired galaxies likely ionized by pAGB stars, independent of their position on the BPT diagram (see the $\text{EW}(\text{H}\alpha)$ colour scale values in Figs 8 and 9) and $\text{H}\alpha + [\text{N II}]$ emission morphology. Only in ESO0507-G025 and NGC 677 do we see clear indications of AGN activity in the nuclear region from the WHAN diagram, with the $\text{EW}(\text{H}\alpha) \sim 3\text{--}6 \text{ \AA}$ indicating a weak AGN. However, some galaxies in our sample have clear signatures of AGN activity as reported in studies at other wavelengths. For example, NGC 4261 is the brightest galaxy in the NGC 4261 group. *Hubble Space Telescope (HST)* WFPC2 observations (Jaffe et al. 1993) and our MUSE data reveal a bright nuclear optical source surrounded by a disc of gas and dust, while radio observations identified two jets perpendicular to the disc

(Birkinshaw & Davies 1985; Scheneider 2006; Kolokythas et al. 2015). Recent kinematical studies using ALMA CO (Boizelle et al. 2021) find a dynamical mass for the central supermassive black hole (BH) in NGC 4261 of $1.67 \times 10^9 M_\odot$. So, the observed LINER properties in this galaxy may be explained by an obscured low-luminosity AGN (Zezas et al. 2005). In addition, 17/18 galaxies in our sample show detected radio continuum emission (Kolokythas et al. 2018); 4/18 show small (≤ 20 kpc; NGC 1060 and NGC 5846) and large-scale (> 20 kpc; NGC 193 and NGC 4261) jets; 3/10 diffuse (NGC 677, NGC 1587, and ESO0507-G025), and 10/18 a point-like or unresolved point source radio continuum morphology (≤ 11 kpc; NGC 410, NGC 584, NGC 777, NGC 924, NGC 940, NGC 978, NGC 1453, NGC 4008, NGC 4169, and NGC 7619).

The results in this section indicate that $\text{EW}(\text{H}\alpha)$, $\log [\text{N II}]/\text{H}\alpha$, and the BPT diagrams, alone, cannot distinguish between dominant ionizing sources producing the central and extended LINER-like emission in our sample. However, the overall $\log [\text{N II}]/\text{H}\alpha$ (Fig. 5) shows that this emission-line ratio decreases as the extent of the emission-line region increases, indicating that *the ionization sources are having different impacts at different radii*. The same decreasing value with the distance pattern is observed for $\sigma([\text{N II}])$, the $12 + \log(\text{O}/\text{H})$ abundances and in most cases the $\text{EW}(\text{H}\alpha)$. The central regions are almost certainly influenced by low-luminosity AGNs, while the extended regions are ionized by other mechanisms (SF and/or cooling flows shocks and pAGBs). The $\text{EW}(\text{H}\alpha)$ in the outer parts is in the range of $0.5\text{--}2.4 \text{ \AA}$ (see Fig. 7), thus indicating that pAGBs are likely contributing significantly to the ionization of these regions. Finally, our interpretations are based on the comparison with models. Factors like L_{yc} photon escape and dilution of nuclear EWs (Papaderos et al. 2013) have not been considered. Consequently, the addition of these processes may constitute an important element in understanding of ETGs with extended optical LINER-like emission.

4.3 Gas-phase abundances $12 + \log(\text{O}/\text{H})$ and metallicity gradients

Warm gas-phase abundances in our sample are difficult to obtain at optical wavelengths due to the uncertainty about the ionization mechanism (see Section 1 and previous results in Section 4.2). The wavelength range covered by MUSE does not allow the detection of $[\text{O II}] \lambda 3727$ and $[\text{O III}] \lambda 4363$. Therefore, the $12 + \log(\text{O}/\text{H})$ abundance in each nuclear region was derived using linear interpolation between the models (AGN, pAGBs, and X-ray emission) and their measured emission-line ratios ($\log([\text{O III}]/\text{H}\beta)$ and $\log([\text{N II}]/\text{H}\alpha)$). Additionally, we used the following calibrators: (i) AGN calibration (AGN N2 calibrator) proposed by Carvalho et al. (2020):

$$12 + \log\left(\frac{\text{O}}{\text{H}}\right) = 12 + \log\left(\frac{Z}{Z_\odot} \times 10^{\log\left(\frac{\rho}{\rho_\odot}\right)}\right), \quad (2)$$

where $Z/Z_\odot = 4.01^{N2} - 0.07$ for $0.3 < (Z/Z_\odot) < 2.0$, and $N2 = \log([\text{N II}] \lambda 6584/\text{H}\alpha)$. Although this calibration was developed for Seyfert 2 nuclei, it has been used to derive the O/H abundance in narrow-line AGN regions and LINERs (e.g. Krabbe et al. 2021; do Nascimento et al. 2022). (ii) most of our extended regions lie to the right of the empirical Kauffmann et al. (2003) boundary line on the BPT diagrams in Figs 4 and C1 (Appendix C). The O3N2 ratio was suggested by Kumari et al. (2019) as a metallicity tracer of DIG and LI(N)ERs ($\text{EW}(\text{H}\alpha) < 3 \text{ \AA}$) since these regions are likely ionized by pAGB stars, star-forming clusters, and weak AGNs. Therefore, the

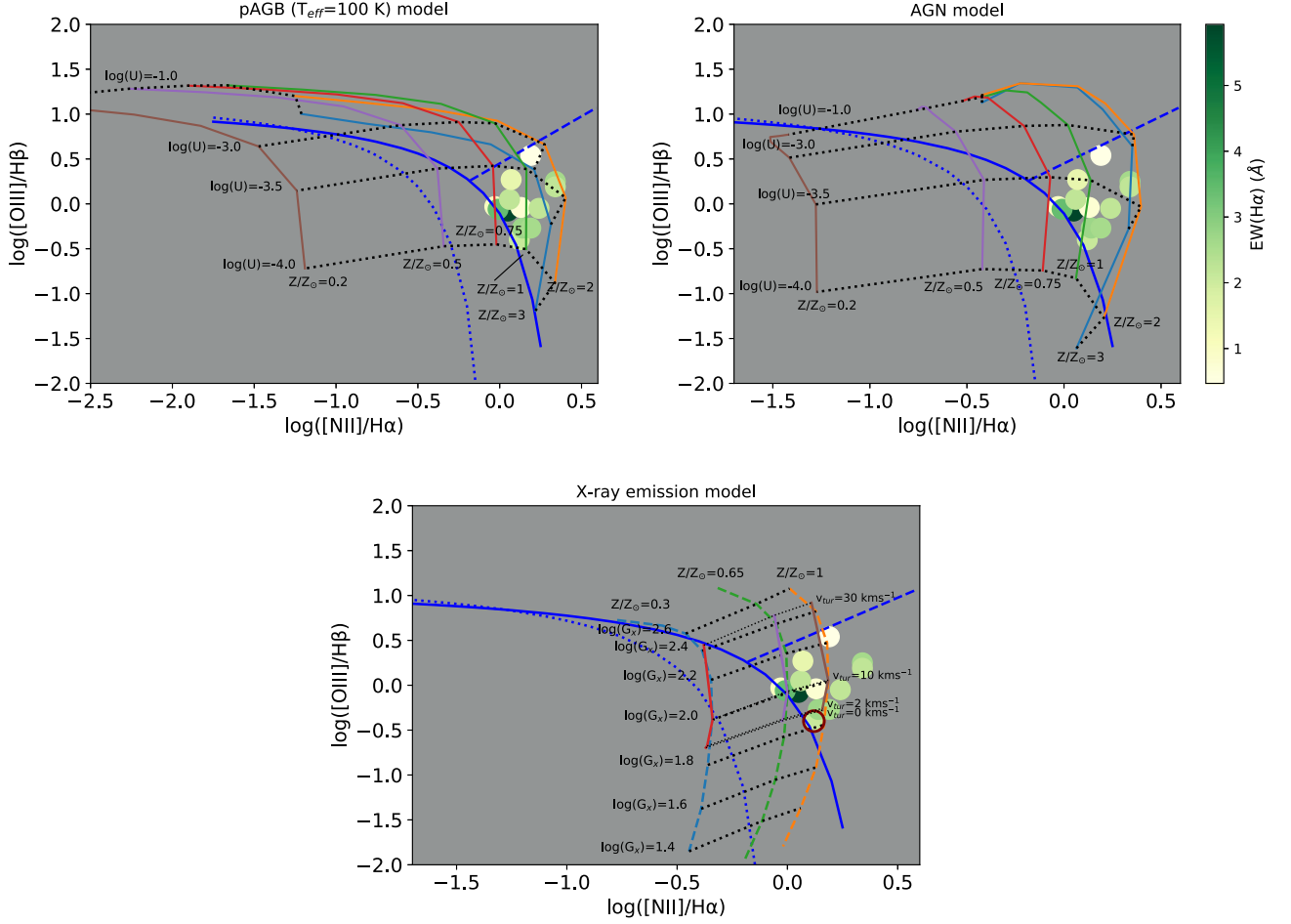


Figure 9. BPT $[\text{O III}]/\text{H}\beta$ versus $[\text{N II}]/\text{H}\alpha$ diagnostic diagrams for several photoionization models. Upper panels: The coloured lines represent the photoionization models from Krabbe et al. (2021) considering pAGB stars (left-hand panel) and AGN activity (right-hand panel) for metallicities from $Z/Z_{\odot} = 0.2$ to 3. The black dotted lines correspond to different ionization parameters from $\log(U) = -1$ to 4.0. Bottom panel: The coloured lines represent photoionization models from Polles et al. (2021) for three metallicities $Z/Z_{\odot} = 0.3, 0.65,$ and 1 considering the variation of X-ray emission $\log(G_x)$ from 2.8 to 1.4 in steps of 0.2 dex (dotted coloured lines and dotted black lines) and including turbulence velocity $v_{\text{turb}} = 30, 10, 2,$ and 0 km s^{-1} (solid coloured lines and small dotted black lines). In these models the optical depth $A_V = 0.1$ mag. The fill colour of the circles indicates the $\text{EW}(\text{H}\alpha)$. The position of NGC 5846 is indicated by the open maroon circle. We superimposed in blue the Kewley et al. (2001; solid line), Kauffmann et al. (2003; dotted line), and Schawinski et al. (2007; dashed line) boundaries as in Fig. 5.

abundances in these regions can be estimated by

$$12 + \log\left(\frac{\text{O}}{\text{H}}\right) = 7.673 + 0.22 \times \sqrt{25.25 - 9.072 \times \text{O3N2}} + 0.127 \times \text{O3}, \quad (3)$$

with $\text{O3N2} = \log([\text{O III}] \lambda 5007/\text{H}\beta \times \text{H}\alpha/[\text{N II}] \lambda 6584)$ and $\text{O3} = \log([\text{O III}] \lambda 5007/\text{H}\beta)$.

Finally, (iii) we compare those values with the ones inferred from the N2 diagnostic, calibrated by Marino et al. (2013) (star-forming H II calibrator) obtained using empirically calibrated direct abundance data (T_e -based measurements) from H II regions in the CALIFA survey. The Marino et al. (2013) calibration is defined as

$$12 + \log\left(\frac{\text{O}}{\text{H}}\right) = 8.743 + 0.462 \times \text{N2}. \quad (4)$$

We note that the emission-line ratios used in any of these relations are not highly affected by reddening.

In Table 5, we show the oxygen abundance for the nuclear 3 arcsec region of each galaxy using the aforementioned methods and their distributions are shown in Fig. 11. In the figure and table we see

that the $12 + \log(\text{O}/\text{H})$ derived from the AGN model and the AGN N2 calibrator are in agreement within the uncertainties (of ± 0.1 dex) with those inferred from the H II calibration in ~ 62 per cent (8/13) and ~ 89 per cent (16/18) of the galaxies, respectively. These values drop to ~ 38 per cent (5/13) and ~ 0 per cent (0/13) when compared to pAGB and X-ray emission models, respectively. However, 100 per cent (13/13) of the nuclear DIG/LI(N)ERs abundances are in agreement, at 1σ level, with the H II values. We note that nuclear metallicities obtained from pAGB and X-ray emission models are, in most cases, lower compared to those obtained from the H II-based method. Two of our galaxies are included within the Annibali et al. (2010) sample of ETGs with ionized gas: NGC 1453 and NGC 5846. Those authors found $12 + \log(\text{O}/\text{H}) = 8.55 \pm 0.19$ and 8.84 ± 0.17 using the calibration in Kobulnicky, Kennicutt & Pizagno (1999) for NGC 1453 and NGC 5846, respectively. Our measurements are in reasonable agreement within the errors with those derived by Annibali et al. (2010) considering apertures and the intrinsic differences between the calibrations.

It is important to bear in mind that the N2 metallicity diagnostics are known to have a dependency on the ionization parameter and the

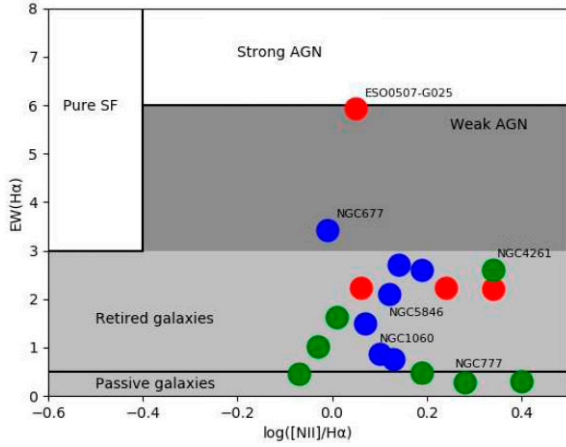


Figure 10. $EW(H\alpha)$ versus $\log [N II]/H\alpha$ (WHAN) diagram. The light and dark grey regions represent the division between gas ionized by weak AGNs and retired galaxies (ionization by pAGBs). The colour of the data points correspond to our $H\alpha + [N II]$ morphological groups: green are type i0, blue are type i, and red corresponds to type ii galaxies.

nitrogen-to-oxygen ratio of the gas, given that metallicities increase with N-enrichment. Unfortunately, we are unable to explore the extended metallicity distribution using methods that do not have a dependence on the aforementioned parameters, given that only the $[N II] \lambda 6584$ and $H\alpha$ emission lines were detected in most of our sample galaxies. On the other hand, the O3N2 method gives nuclear abundances that are in agreement, within the uncertainties, with the ones found using the N2-based abundances. Therefore, we used the N2 and O3N2 indicators, in galaxies with extended $[N II] \lambda 6584$ emission, as a way of obtaining the spatially resolved morphologies of the ionized gas which can be translated into metallicities in a relative rather than absolute way. In Section 3.2, we showed that most spaxels in our spatially resolved BPT maps lie in the AGNs and composite areas of the diagrams. Therefore, we calculated the pixel-by-pixel $12 + \log(O/H)$ abundance in those regions by adopting the

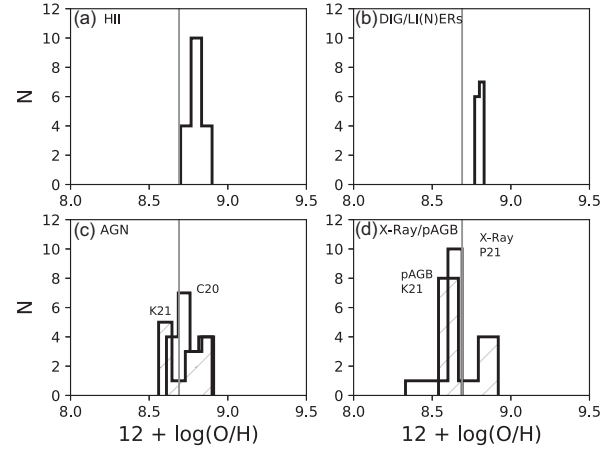


Figure 11. Oxygen abundance distributions for the nuclear SDSS 3 arcsec apertures in panels (a) ionization by stars (H II) using the N2 calibration by Marino et al. (2013). Panel (b) shows the abundances from DIG/LI(N)ERs O3N2 calibration by Kumari et al. (2019), respectively. Panel (c) shows the distribution of abundances from AGN photoionization model (Krabbe et al. 2021; K21) and Carvalho et al. (2020; C20) calibration. Panel (d) shows the same but considering pAGB photoionization (K21) and X-ray (Polles et al. 2021; P21) models. The vertical grey lines indicate the solar abundance $12 + \log(O/H)_{\odot} = 8.69$.

Carvalho et al. (2020) (AGN N2; green dots) and Kumari et al. (2019) (DIG/LI(N)ERs O3N2; blue dots) calibrators. While values from the N2 calibration by Marino et al. (2013) (H II; black dots) are included for comparison. In Fig. 12, we show for each galaxy in our sample the $12 + \log(O/H)$ abundances as function of the radius from the galaxy's centre. The dots are the median values within circular bins of 1.5 arcsec radii, except for the first bin which has a radius of 0.5 arcsec. The error bars, in this figure, denote the 1σ distribution of the H II $12 + \log(O/H)$ per bin.

In Fig. 12, we see that the calibrators predict comparable metallicities but with a small offset (≤ 0.1 dex in most cases) in the innermost regions, while for the extended regions this difference can

Table 5. Oxygen abundance determinations for the nuclear region (3 arcsec aperture) assuming pure H II regions (Marino et al. 2013; H II), AGN models (Krabbe et al. 2021), and the AGN N2-based calibrator (Carvalho et al. 2020), the DIG/LI(N)ERs O3N2 calibrator (Kumari et al. 2019; DL), and pAGB (Krabbe et al. 2021) and X-ray (Polles et al. 2021) emission models, respectively.

	$12 + \log(O/H)_{H II}$ N2	$12 + \log(O/H)_{AGN}$ model	$12 + \log(O/H)_{DL}$ O3N2	$12 + \log(O/H)_{pAGB}$ model	$12 + \log(O/H)_{X-ray}$ model
NGC 193	8.81 ± 0.09	8.76 ± 0.16	8.75 ± 0.10	8.82 ± 0.10	8.63 ± 0.16
NGC 410	8.75 ± 0.05	–	8.66 ± 0.07	–	–
NGC 584	8.80 ± 0.10	8.71 ± 0.16	8.74 ± 0.11	8.81 ± 0.16	8.60 ± 0.17
NGC 677	8.74 ± 0.08	8.56 ± 0.08	8.65 ± 0.10	8.78 ± 0.10	8.55 ± 0.05
NGC 777	8.87 ± 0.13	–	8.84 ± 0.13	–	–
NGC 924	8.77 ± 0.07	8.57 ± 0.11	8.70 ± 0.08	8.79 ± 0.15	8.55 ± 0.12
NGC 940	8.90 ± 0.11	8.90 ± 0.10	8.88 ± 0.10	8.83 ± 0.17	8.92 ± 0.17
NGC 978	8.71 ± 0.07	8.56 ± 0.01	8.64 ± 0.08	8.77 ± 0.08	8.55 ± 0.03
NGC 1060	8.79 ± 0.12	–	8.72 ± 0.14	–	–
NGC 1453	8.83 ± 0.06	8.83 ± 0.06	8.78 ± 0.05	8.83 ± 0.10	8.74 ± 0.14
NGC 1587	8.78 ± 0.06	8.59 ± 0.11	8.70 ± 0.07	8.77 ± 0.08	8.54 ± 0.10
NGC 4008	8.71 ± 0.12	–	8.61 ± 0.15	–	–
NGC 4169	8.85 ± 0.06	8.85 ± 0.04	8.81 ± 0.05	8.83 ± 0.12	8.81 ± 0.10
NGC 4261	8.90 ± 0.13	8.90 ± 0.13	8.88 ± 0.12	8.83 ± 0.19	8.91 ± 0.26
ESO0507-G025	8.76 ± 0.06	8.57 ± 0.08	8.69 ± 0.07	8.79 ± 0.14	8.55 ± 0.07
NGC 5846	8.80 ± 0.10	8.75 ± 0.18	8.74 ± 0.11	8.83 ± 0.09	8.59 ± 0.16
NGC 6658	8.83 ± 0.11	8.81 ± 0.28	8.78 ± 0.11	8.78 ± 0.31	8.81 ± 0.32
NGC 7619	8.93 ± 0.20	–	8.91 ± 0.22	–	–

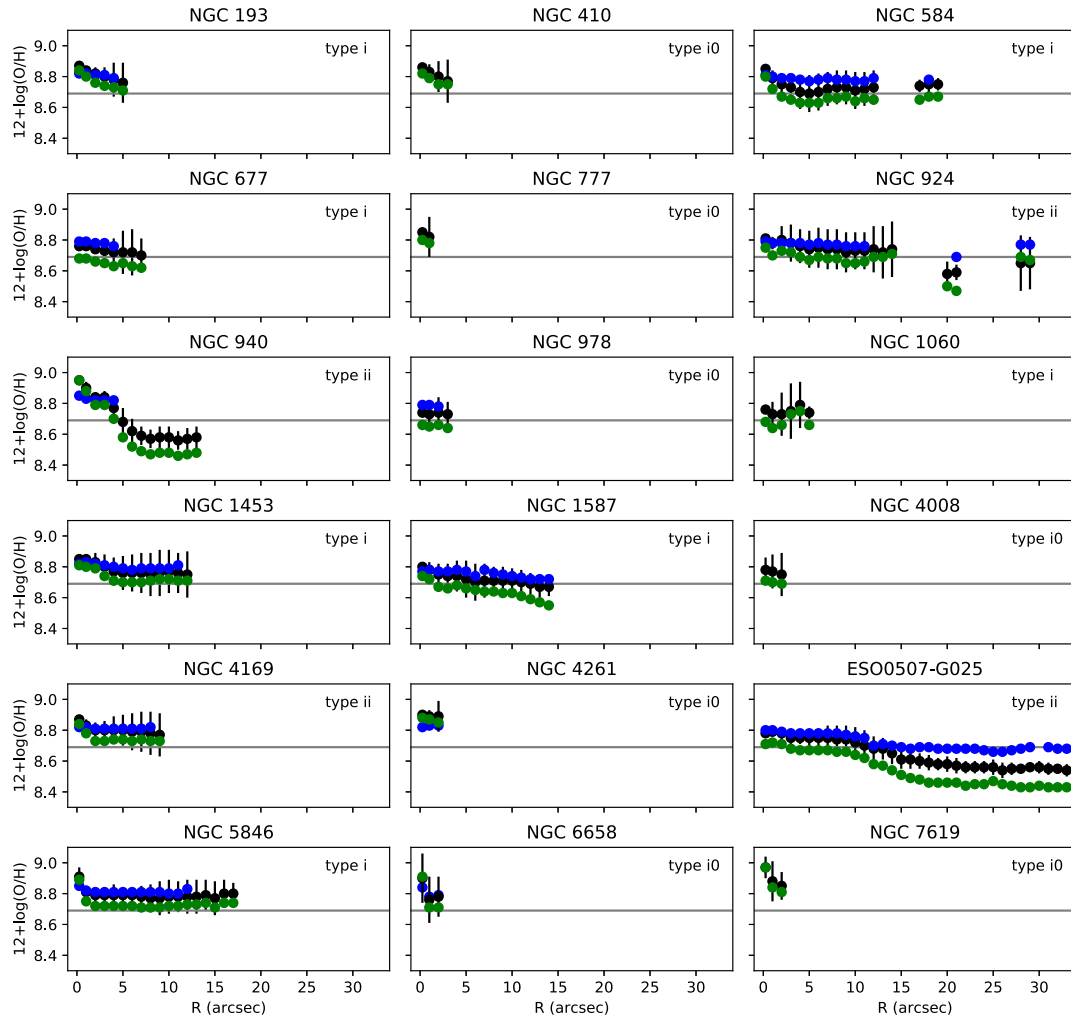


Figure 12. $12 + \log(\text{O}/\text{H})$ profiles for the sample galaxies by adopting the N2 calibrations by Marino et al. (2013) (H II; black data points), Carvalho et al. (2020) (AGNs; green data points), and Kumari et al. (2019) (DIG/LI(N)ERs; blue data points). The data points correspond to the median $12 + \log(\text{O}/\text{H})$ from bins in steps of 1.0 arcsec radii, except the central bin which is 0.5 arcsec. The error bars denote the 1σ distribution of the y-values per each bin. The solar abundance $12 + \log(\text{O}/\text{H})_{\odot} = 8.69$ is indicated by the grey horizontal lines.

reach values of ~ 0.3 dex in the case of ESO0507-G025. From this figure it is clear that there is a break in the metallicity gradient with a very steep gradient in the central region which, as indicated in Section 4.2, is more influenced by low-luminosity AGNs. We calculated the metallicity gradient ($\nabla_{\text{O}/\text{H}}$) as the slope of the linear fit to the median $12 + \log(\text{O}/\text{H})$ values separately for the innermost and extended regions for all the calibrations considered. In Table F1 (Appendix F available as supplementary online material), we present for each galaxy the results of our linear fitting and statistics of all pixels/spaxels used to create the $12 + \log(\text{O}/\text{H})$ profiles. From this table, we see that the central metallicity gradients are in all cases negative, while the extended regions show a flat gradient.

4.4 Properties of the gas and its origin

4.4.1 Properties of the gas and metallicity gradients

From the previous section, we see that the mean gas-phase metallicity in the nuclear and extended regions are $\langle (\text{O}/\text{H})_{\text{nuclear}} \rangle > \langle (\text{O}/\text{H})_{\text{extended}} \rangle$ with the $12 + \log(\text{O}/\text{H})$ abundance generally decreasing with radius, independently of the ionization source or method considered, with

a flattening of metallicity gradients for the outermost regions. In Fig. 13, we show the relationship between metallicity gradients $\nabla_{\text{O}/\text{H}}$ for the central and extended regions and $\text{H}\alpha + [\text{N II}]$ morphology of our sample. In Table 6, we summarize the average metallicity gradients for each region and calibrator considered. A weak positive Spearman's correlation ~ 0.6 between metallicity gradients and morphological $\text{H}\alpha + [\text{N II}]$ types of the galaxies is found in Fig. 13. Despite the low number statistics in our study, these results suggest that the nuclear $\nabla_{\text{O}/\text{H}}$ of type i group-dominant galaxies, on average, is lightly higher than type i0 and type ii galaxies. However, the intrinsic uncertainties associated with these values lead us to consider the metallicity gradients may not be statistically significant. Therefore, we argue that the similarity in the shape of the nuclear metallicity gradients in all galaxy types and the flattening of the outer regions in our sample of group-dominant galaxies with type i (strong nuclear emission plus extend filamentary structures) and type ii (strong or diffuse nuclear emission plus extranuclear H II regions) morphologies are a common property in this group of galaxies. Several groups (e.g. Sánchez et al. 2014; Belfiore et al. 2017, and references therein) have studied the metallicity gradients in local galaxy samples. In Sánchez et al. (2014) and Sánchez (2020), they show that a significant fraction

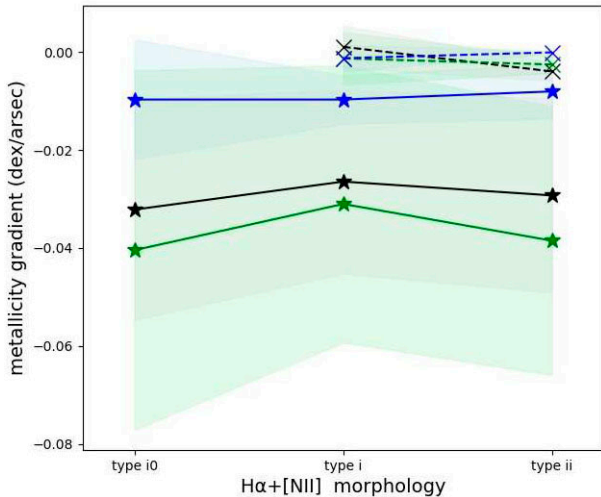


Figure 13. Relationship between metallicity gradients $\nabla_{O/H}$ and $H\alpha+[NII]$ morphology of the galaxies. More details about the classes of emission-line morphology are given in Section 3.1. The horizontal lines indicate the average of the metallicity gradients $\nabla_{O/H}$ for central (stars) and extended (crossed) fit components considering three different calibrators for H II regions (black; Marino et al. 2013), AGNs (green; Carvalho et al. 2020) and DIG/LIERs (blue; Kumari et al. 2019). The standard deviation for each quantity is indicated by the filled regions.

of galaxies in the CALIFA sample exhibit shallow metallicity slopes in their innermost and/or outermost regions. In particular, they argue that the flattening in the outer regions is a universal property of disc galaxies, which is independent of the inclination, mass, luminosity, morphology, and the presence of bars. In this and other similar works, several mechanisms like radial motion, inside-out growth, metal-poor/rich gas accretion, turbulent transport, and outflow of gas (e.g. Kewley et al. 2010; Sánchez-Menguiano et al. 2018; Sánchez 2020, see references therein) are invoked as the sources of producing the gas metallicity profiles.

The properties of the extended warm ISM in our sample of type i and type ii galaxies suggest, within the uncertainties, nearly solar (± 0.2 dex) homogeneous chemical abundances (see Fig. 12 and Table F1). This likely requires mechanisms (e.g. radial motions, gas-clouds or satellite accretion/interactions, AGN/SF-driven outflows) for the efficient gas transport, mixing, and radial flattening of metallicity into the outer regions of the galaxies in a relative short time-scale (e.g. Werk et al. 2011; Bresolin, Kennicutt & Ryan-Weber 2012; Rennehan et al. 2019; Rennehan 2021), likely similar to other low-redshift galaxy classes.

4.4.2 Cold gas content

H I is a sensitive tracer of external environmental mechanisms in galaxies. A study of H I in ETGs by Serra et al. (2012) found that H I detections were relatively uncommon near Virgo cluster centre (10 per cent) but were common (40 per cent) in field with the detected H I mass inversely related to environment density. H I morphology was also found to vary in a continuous way from regular, settled H I discs and rings in the field to unsettled gas distributions (including tidal or accretion tails) at the Virgo cluster centre, with the H I and CO-richest galaxies found in the poorest environments where the SF detection rate was also higher. This implies that galaxy group processing is involved in evolving pre-existing ETG gas properties.

In our sample, 8/18 galaxies have the H I properties available from the literature and 18/18 have been observed in CO (see our Table G1 in Appendix G, available as supplementary online material, for a summary; O’Sullivan et al. 2015, 2018). In Fig. G1, we show single-dish H I spectra from the literature for seven of these galaxies. Excluding the two galaxies in Table G1 which have a caveat about their H I properties (see Table G1 note in Appendix G) the mean H I in type ii galaxies is $17.2 \times 10^9 M_{\odot}$ compared to the mean H I in type i galaxies of $1.4 \times 10^9 M_{\odot}$, i.e. the type ii have an order of magnitude more H I. NGC 940 was excluded from the above calculation because of the high uncertainty about its H I detection, however it has a large $M(H_2)$ mass ($6.1 \times 10^9 M_{\odot}$). The H_2 mass of NGC 940 together with the H I masses of the other type ii galaxies confirms that the type ii galaxies are cold gas rich. To varying degrees, all the H I in our galaxies display double-horned H I profiles which are indicative of rotating discs, with the clearest examples being NGC 924 and NGC 940 which also have the lowest H I profile asymmetries as measured by the A_{flux} parameter (Espada et al. 2011).

It seems likely the cold and warm discs in the type ii galaxies are part of the same kinematical gas structures, with support for this coming from the H I profiles and the [N II] velocity fields in Fig. 6 and Appendix D. In the [N II] velocity fields we see that all of the type ii galaxies show clear rotating disc patterns, with NGC 940 presenting a highly symmetric case. The high levels of symmetry in the velocity fields, especially in NGC 940, together with the flattened metallicity gradients argue against the gas having been recently acquired. In particular, using Romulus hydrodynamic cosmological simulations Jung et al. (2022) examined the re-emergence of gaseous and stellar discs in BGGs following their destruction by mergers. They find that ordered discs take ~ 1 Gyr to be established. We suggest that our gas-rich systems obtained their cold gas at least ~ 1 Gyr ago (Holwerda et al. 2011; Jung et al. 2022), i.e. the H I virialization time-scale after gas-clouds or satellite mergers/accretion. However, we observe that $\sigma_{gas, central} \gtrsim \sigma_{gas, extended}$, so the warm gas in the central regions is unlikely to be dynamically relaxed (Olivares et al. 2022) in the gravitational potential of the galaxy, indicating an AGN outburst contribution. Those results are in agreement with the morphology of the warm gas distribution and velocity fields observed in our sample (Section 3.3).

4.4.3 Summary of properties, chemical abundances, and possible scenarios for the origin of the gas in group-dominant galaxies

The interpretation of internal (stellar mass-loss) and external mechanisms (cooling from the IGrM or mergers/interactions) for the origin of the gas in our sample is difficult, since different mechanisms could be acting at different evolutionary stages. Kolokythas et al. (2022) examined the relationships between radio power, SFR (FUV), and stellar mass for CLoGS, which includes our analysed galaxies, and find no correlations between these quantities. This suggests a mix of origins for the cool gas in these systems, including stellar mass-loss, cooling from the IGrM/galaxy halo, settling gas due to mergers, and tidal or ram pressure stripping (see also Loubser et al. 2022). In systems like NGC 978 and NGC 1587 the observed ionized gas (see Appendix B) could be associated with an interaction with the companion galaxy. Although no cold gas has been reported in NGC 978, the interaction debris gas may eventually enter the galaxy’s (hot) halo to trigger the SF and feed the AGN activity. On the other hand, the SF in extranuclear regions (type ii galaxies) is likely a later stage after streams gas settling from orbiting satellites (Jung et al. 2022). Kolokythas et al. (2022) argued that S0 group-dominant

Table 6. Average and standard deviation (sd) metallicity gradients ($\nabla_{(O/H)}$), in units of dex arcsec⁻¹, for the central and extended regions (left and right values in each column) using the calibrators H II N2 regions (Marino et al. 2013), AGN N2 (Carvalho et al. 2020), and O3N2 DIG/LI(N)ERs (Kumari et al. 2019).

	H II N2		AGN N2		DIG/LIERs O3N2	
	Central ($\nabla_{(O/H)}$)/sd	Extended ($\nabla_{(O/H)}$)/sd	Central ($\nabla_{(O/H)}$)/sd	Extended ($\nabla_{(O/H)}$)/sd	Central ($\nabla_{(O/H)}$)/sd	Extended ($\nabla_{(O/H)}$)/sd
type i0	-0.032/0.022	–	-0.040/0.037	–	-0.010/0.012	–
type i	-0.026/0.019	0.0011/0.0043	-0.031/0.028	-0.0013/0.0053	-0.010/0.005	-0.0012/0.0027
type ii	-0.029/0.020	-0.0039/0.0019	-0.038/0.027	-0.0025/0.0017	-0.008/0.005	-0.0000/0.0003

galaxies (type ii galaxies) occupy X-ray-faint systems and have point-like radio sources (Kolokythas et al. 2018), which indicates that the cold gas is more likely to be the result of gas-rich mergers or tidal interactions instead of cooling from a hot IGrM. While in some type i galaxies (as in the case of NGC 5846 where the ionized gas morphology supports a cooling flow) the cooled gas from the IGrM may be an effective mechanism forming filaments and rotating discs in the galaxy nuclei (O’Sullivan et al. 2015; Olivares et al. 2022, and references therein). Three-fourths of the galaxies (NGC 193, NGC 1060, and NGC 5846) with radio jet-like morphology present filamentary ionized gas structures characteristic of ICM cooling. The presence of misaligned or counterrotating ionized gas discs with respect to the stellar body is a strong indication of external accretion of gas. We find direct evidence of this; Olivares et al. (2022) found that most of the galaxies in our sample have ionized gas kinematically decoupled from the stellar component, which suggests an external origin of the gas. Observational evidence (e.g. Sarzi et al. 2006; Gomes et al. 2016) and simulations (Starkenburger et al. 2019; Kim et al. 2021; Jung et al. 2022, among others) indicate possible origins of this misalignment in galaxies regardless of the morphology and environment, with early-type having higher misaligned fractions. We argue that stellar mass-loss is unlikely to be the dominant source of cold gas in our sample (see Olivares et al. 2022).

If we assume that the metallicity of the warm gas, in our sample, is represented by a single calibrator (AGN N2 or DIG/LI(N)ERs O3N2), on average, the nuclear regions are more metal rich than their extended structures, i.e. $\langle(O/H)_{\text{nuclear}}\rangle \gtrsim \langle(O/H)_{\text{extended}}\rangle$. However, in Section 4.2 we find that the ionization sources are having different impacts at different radii. Therefore, the abundance in the nuclear regions is well represented by the 3 arcsec apertures and they can be obtained as the average between the AGN N2 and the interpolated AGN abundances from the models (Fig. 9), while for the extended regions the average abundances are from the data points in Section 4.3 (see Table F1) assuming the DIG/LI(N)ERs O3N2 calibrator. This is a reasonable assumption given that most of the spaxels in these regions are in the composite area of the BPT diagrams. In Table 7, we summarize and compare the gas-phase metallicities ($Z = [O/H] = \langle \log(O/H) \rangle - \langle \log(O/H)_{\odot} \rangle$) found in this work with those in the IGrM by O’Sullivan et al. (2017). In the nuclear regions the metallicities range from ~ 0.9 to $1.7 Z_{\odot}$. The metallicity in the extended structures often rise to values approaching the solar $\sim 1.0 Z_{\odot}$ or higher (≤ 0.3 dex), while the IGrM has metallicities down to ~ 0.1 – $0.7 Z_{\odot}$. In the case of NGC 940, NGC 4261, and NGC 7619 the nuclear metallicities are $\gtrsim 0.6$ dex higher than the solar value. Interestingly, in four cases (NGC 584, NGC 1587, ESO0507-G025, and NGC 5846), we found a drop in the nuclear metallicity with respect to the extended regions of ≤ 0.2 dex in NGC 584 and NGC 5846 and ~ 0.1 dex for NGC 1587 and ESO0507-G025. This suggest the accretion of metal-poor gas to the central AGN (e.g. do Nascimento et al. 2022). Since metallicity in the nuclear regions represent the average metallicity within the 3

Table 7. Comparison between Z (this work) and IGrM metallicities in units of Z/Z_{\odot} . Column (1): average value between the AGN N2 and interpolated abundances from the AGN models. Column (2): abundances in the extended regions from DIG/LI(N)ERs O3N2 calibrator. Column (3) corresponds to IGrM metallicity from O’Sullivan et al. (2017).

	Nuclear 3 arcsec AGN (1)	Extended DIG/LI(N)ERs (2)	IGrM (3)
NGC 193	1.15	–	0.68
NGC 410	0.94	–	0.42
NGC 584	1.08	1.35	–
NGC 677	0.84	–	0.38
NGC 777	1.41	–	0.63
NGC 924	0.89	0.85	–
NGC 940	1.57	1.07	0.06
NGC 978	0.82	–	>0.29
NGC 1060	1.08	–	0.28
NGC 1453	1.30	1.29	0.42
NGC 1587	0.91	1.05	0.03
NGC 4008	0.84	–	0.32
NGC 4169	1.38	1.35	0.11
NGC 4261	1.58	–	0.23
ESO0507-G025	0.88	0.98	–
NGC 5846	1.12	1.32	0.27
NGC 6658	1.27	–	<0.18
NGC 7619	1.67	–	0.54

arcsec apertures and the uncertainties on the abundances are of the order of ~ 0.1 dex, we find in our sample of group-dominant galaxies that $Z_{\text{nuclear}} \gtrsim Z_{\text{extended}} > Z_{\text{IGrM}}$.

The mixing and dispersion of heavy elements in the ISM of galaxies, in general, should follow the ‘evolutionary’ stages of disc growth at different spatial scales. It might be suggested, in our case, by a correlation between gas-phase metallicity gradients $\nabla_{O/H}$ and $H\alpha + [N II]$ morphology (see Fig. 13), since the effect of gas flows over the lifetime of the galaxies seems to produce the flattening of abundances out to large radii (e.g. Kewley et al. 2010; Sánchez et al. 2014; López-Sánchez et al. 2015), following the formation of the extended structures. However, we find no correlation between the metallicity gradients and morphology (Section 4.4.1) in our sample of BGGs. This is in agreement with the idea of relatively short time-scales for the radial dispersion and mixing of metals to large spatial scales likely produced by the AGN/SF-driven outflows, gas accretion, and mergers/interactions. Furthermore, some of these metals will be transported by these mechanisms from the galaxies into the IGrM/ICM. In particular, group-dominant galaxies often host radio AGNs that are interacting with the surrounding gas by forming cavities and shock fronts (see Olivares et al. 2022, for a description of these structures in our sample). As seen in Section 3.3, we observe large gas velocity dispersion in the central regions of

the galaxies, likely associated with the presence of AGN activity. Therefore, group-dominant galaxies likely acquired their cold gas as a consequence of several possible mechanisms, i.e. gas-clouds or satellite mergers/accretion and cooling flows which together with the AGN/SF activity are likely contributing to the growth of the ionized gas structures and flattening the metallicity gradients.

5 CONCLUSIONS

In this paper, we present archival MUSE observations for a sample of 18 group-dominant galaxies from the CLoGS sample (O’Sullivan et al. 2017). We derive and removed the stellar continuum for all galaxies by fitting the stellar SEDs using the spectral synthesis code FADO (Gomes & Papaderos 2017). We studied the properties (i.e. emission-line ratios, chemical abundances, etc) and structure of the warm gas, in each galaxy, in order to constrain the ionization processes, the origin of their gas, and its chemical abundance distribution. We summarize our main results as follows:

(i) We used the continuum-subtracted $H\alpha + [N II]$ images (see Fig. 3) to classify the galaxies into three morphological groups or types: *type i0* – strong or diffuse nuclear emission with (or without) unextended filamentary ($\lesssim 1$ kpc) structures connected to the nuclear region, *type i* – strong or diffuse nuclear emission with extended (several kpc) filamentary structures beyond the nuclear region, and *type ii* – i0 or i plus extranuclear HII regions (well-defined or in distorted ring-like structures). We find that 5/18 (NGC 410, NGC 978, NGC 4008, NGC 4261, and NGC 6658) are type i0, 9/18 of these objects are type i (NGC 193, NGC 584, NGC 677, NGC 777, NGC 1060, NGC 1453, NGC 1587, NGC 5846, and NGC 7619), and 4/18 galaxies are type ii (NGC 924, NGC 940, NGC 4169, and ESO0507-G025).

(ii) In order to distinguish between different ionization mechanisms, in Section 3.2 we used the following emission-line ratios $[O III]/H\beta$ and $[N II]/H\alpha$ and the equivalent width $EW(H\alpha)$. The spatially resolved $\log [N II]/H\alpha$ ratios decrease as the extent of the emission-line region increases, indicating that the sources of the ionization are acting at different spatial scales. The same decreasing pattern with the distance is observed for the velocity dispersion $\sigma([N II])$, the $12 + \log(O/H)$ abundances, and in most cases the $EW(H\alpha)$. Using emission-line diagnostic diagrams (or BPT diagrams) we find that all galaxies in our sample have a dominant LINER/AGN nuclear region. Extended LINER-like regions are observed in most galaxies with filamentary structures. In the same section, we studied the mechanisms (pAGBs, AGNs, and X-ray emission) responsible for the ionization which produces the optical emission lines in our sample. Although AGNs, pAGBs, and X-ray emission models are able to reproduce the observational data, we suggest that the central regions are more influenced by low-luminosity AGNs, while the extended regions are ionized by other mechanisms with pAGBs photoionization likely contributing significantly as suggested by their $EW(H\alpha)$ values.

(iii) We calculated the gas-phase metallicity ($12 + \log(O/H)$) using linear interpolations between the AGNs, pAGBs, and X-ray emission models (Krabbe et al. 2021) and their measured emission-line ratios ($\log([O III]/H\beta)$ and $\log([N II]/H\alpha)$). We also used the AGN N2 (Carvalho et al. 2020) and DIG/LI(N)ERs O3N2-based (Kumari et al. 2019) calibrators. Using a single calibrator (AGN N2 or DIG/LI(N)ERs O3N2), the $12 + \log(O/H)$ in the nuclear and extended regions (see Fig. 12) are $\langle (O/H)_{\text{nuclear}} \rangle \gtrsim \langle (O/H)_{\text{extended}} \rangle$. We found that the metallicity gradients for the pixel-by-pixel data points are, in most cases, negative in the innermost regions with a flat

gradient for the extended areas beyond the centre, which includes extended structures and some star-forming regions. In this sense, the morphological $H\alpha + [N II]$ types defined in this study indicate that group-dominant galaxies with extended filamentary structures (type i) and S0 galaxies with extranuclear SF regions (type ii), on average, have shallow metallicity gradients. Therefore, the extended regions and ring-like structures of ionized gas can be considered chemically homogeneous (nearly solar) within the uncertainties. If the ionization sources have different impacts at different radii (as seen in Section 3.2) we use the AGN N2 calibrator and AGN models to estimate the nuclear (3 arcsec aperture) abundances and the DIG/LI(N)ERs O3N2 calibrator for the extended regions. Therefore, we found in NGC 584, NGC 1587, ESO0507-G025, and NGC 5846 a slight drop in the nuclear metallicity with respect to the extended regions, suggesting the accretion of metal-poor gas to the central regions. However, we find within the uncertainties that $Z_{\text{nuclear}} \gtrsim Z_{\text{extended}} > Z_{\text{IGRM}}$.

(iv) We suggest that group-dominant galaxies likely acquired their cold gas in the past as a consequence of one or more external mechanisms where gas-clouds or satellite mergers/accretion (Section 4.4.2) and cooling flows are likely supplying the gas for the growth of the ionized gas structures and AGN/SF activity. Our results favour a scenario in which metals are distributed across the ISM of the galaxies on short time-scales.

ACKNOWLEDGEMENTS

We thank the reviewer for his/her careful reading of the manuscript and helpful comments which substantially improved the paper. PL (contract DL57/2016/CP1364/CT0010) and TS (contract DL57/2016/CP1364/CT0009) are supported by national funds through Fundação para a Ciência e Tecnologia (FCT) and the Centro de Astrofísica da Universidade do Porto (CAUP). SIL and KK are supported in part by the National Research Foundation of South Africa (NRF Grant Numbers: 120850). Opinions, findings and conclusions, or recommendations expressed in this publication are that of the author(s), and that the NRF accepts no liability whatsoever in this regard. EOS acknowledges support for this work from the National Aeronautics and Space Administration through *XMM-Newton* award 80NSSC19K1056. AB acknowledges support from NSERC through its Discovery Grant Program. PL thanks Polychronis Papaderos for his very useful comments. We thank Angela Krabbe for providing us with the CLOUDY models used in this work. This research has made use of the NASA/IPAC Extragalactic Database (NED), which is funded by the National Aeronautics and Space Administration and operated by the California Institute of Technology.

DATA AVAILABILITY

The data underlying this article will be shared on reasonable request to the corresponding author.

REFERENCES

- Allen M. G., Groves B. A., Dopita M. A., Sutherland R. S., Kewley L. J., 2008, *ApJS*, 178, 20
 Annibali F., Bressan A., Rampazzo R., Zeilinger W. W., Vega O., Panuzzo P., 2010, *A&A*, 519, A40
 Asplund M., Grevesse N., Sauval A. J., Scott P., 2009, *ARA&A*, 47, 481
 Bacon R. et al., 2001, *MNRAS*, 326, 23

- Bacon R. et al., 2010, in McLean I. S., Ramsay S.K., Takami H., eds, Proc. SPIE Conf. Ser. Vol. 7735, Ground-based and Airborne Instrumentation for Astronomy III. SPIE, Bellingham, p. 08
- Baldwin J. A., Phillips M. M., Terlevich R., 1981, *PASP*, 93, 5
- Barth A. J., Ho L. C., Filippenko A. V., Sargent W. L. W., 1998, *ApJ*, 496, 133
- Belfiore F. et al., 2016, *MNRAS*, 461, 3111
- Belfiore F. et al., 2017, *MNRAS*, 469, 151
- Bildfell C., Hoekstra H., Babul A., Mahdavi A., 2008, *MNRAS*, 389, 1637
- Binette L., Magris C. G., Stasińska G., Bruzual A. G., 1994, *A&A*, 292, 13
- Birkinshaw M., Davies R. L., 1985, *ApJ*, 291, 32
- Boizelle B. D. et al., 2021, *ApJ*, 908, 19
- Bresolin F., Kennicutt R. C., Ryan-Weber E., 2012, *ApJ*, 750, 122
- Bruzual G., Charlot S., 2003, *MNRAS*, 344, 1000
- Cappellari M., 2017, *MNRAS*, 466, 798
- Cappellari M., Copin Y., 2003, *MNRAS*, 342, 345
- Cardelli J. A., Clayton G. C., Mathis J. S., 1989, *ApJ*, 345, 245
- Carvalho S. P. et al., 2020, *MNRAS*, 492, 5675
- Chabrier G., 2003, *PASP*, 115, 763
- Cid Fernandes R., Stasińska G., Schlickmann M. S., Mateus A., Vale Asari N., Schoenell W., Sodré L., 2010, *MNRAS*, 403, 1036
- Cid Fernandes R., Stasińska G., Mateus A., Vale Asari N., 2011, *MNRAS*, 413, 1687
- Ciocan B. I., Ziegler B. L., Verdugo M., Papaderos P., Fogarty K., Donahue M., Postman M., 2021, *A&A*, 649, A23
- Crawford C. S., Allen S. W., Ebeling H., Edge A. C., Fabian A. C., 1999, *MNRAS*, 306, 857
- Davis T. A. et al., 2011, *MNRAS*, 417, 882
- do Nascimento J. C. et al., 2022, *MNRAS*, 513, 807
- Donahue M., Voit G. M., 1991, *ApJ*, 381, 361
- Donahue M., de Messières G. E., O'Connell R. W., Voit G. M., Hoffer A., McNamara B. R., Nulsen P. E. J., 2011, *ApJ*, 732, 40
- Dopita M. A., Sutherland R. S., 1995, *ApJ*, 455, 468
- Dopita M. A., Sutherland R. S., 1996, *ApJS*, 102, 161
- Edwards L. O. V., Hudson M. J., Balogh M. L., Smith R. J., 2007, *MNRAS*, 379, 100
- Erroz-Ferrer S. et al., 2019, *MNRAS*, 484, 5009
- Espada D., Verdes-Montenegro L., Huchtmeier W. K., Sulentic J., Verley S., Leon S., Sabater J., 2011, *A&A*, 532, A117
- Fang J. J., Faber S. M., Salim S., Graves G. J., Rich R. M., 2012, *ApJ*, 761, 23
- Ferland G. J., Netzer H., 1983, *ApJ*, 264, 105
- Ferland G. J., Fabian A. C., Johnstone R. M., 1994, *MNRAS*, 266, 399
- Ferland G. J. et al., 2017, *Rev. Mex. Astron. Astrofis.*, 53, 385
- Fogarty K., Postman M., Connor T., Donahue M., Moustakas J., 2015, *ApJ*, 813, 117
- Gastaldello F., Simionescu A., Mernier F., Biffi V., Gaspari M., Sato K., Matsushita K., 2021, *Universe*, 7, 208
- Gomes J. M., Papaderos P., 2017, *A&A*, 603, A63
- Gomes J. M. et al., 2016, *A&A*, 588, A68
- Gozaliasl G., Finoguenov A., Khosroshahi H. G., Mirkazemi M., Erfanianfar G., Tanaka M., 2016, *MNRAS*, 458, 2762
- Heckman T. M., 1980, *A&A*, 87, 152
- Heckman T. M., Baum S. A., van Breugel W. J. M., McCarthy P., 1989, *ApJ*, 338, 48
- Herpich F., Stasińska G., Mateus A., Vale Asari N., Cid Fernandes R., 2018, *MNRAS*, 481, 1774
- Ho L. C., 1999, *Adv. Space Res.*, 23, 813
- Holwerda B. W., Pirzkal N., Cox T. J., de Blok W. J. G., Weniger J., Bouchard A., Blyth S.-L., van der Heyden K. J., 2011, *MNRAS*, 416, 2426
- Jaffe W., Ford H. C., Ferrarese L., van den Bosch F., O'Connell R. W., 1993, *Nature*, 364, 213
- Jung S. L. et al., 2022, *MNRAS*, 515, 22
- Kakkad D. et al., 2018, *A&A*, 618, A6
- Kauffmann G. et al., 2003, *MNRAS*, 346, 1055
- Kennicutt R. C., 1998, *ApJ*, 498, 541
- Kewley L. J., Dopita M. A., Sutherland R. S., Heisler C. A., Trevena J., 2001, *ApJ*, 556, 121
- Kewley L. J., Rupke D., Zahid H. J., Geller M. J., Barton E. J., 2010, *ApJ*, 721, L48
- Khim D., Yi, Sukyoung K., Pichon C., Dubois Y., Devriendt J., Choi H., Bryant J.J., Croom S.M., 2021, *ApJS*, 254, 27
- Kobulnicky H. A., Kennicutt R. C., Pizagno J. L., 1999, *ApJ*, 514, 544
- Kolokythas K., O'Sullivan E., Giacintucci S., Raychaudhury S., Ishwara-Chandra C. H., Worrall D. M., Birkinshaw M., 2015, *MNRAS*, 450, 1732
- Kolokythas K., O'Sullivan E., Raychaudhury S., Giacintucci S., Gitti M., Babul A., 2018, *MNRAS*, 481, 1550
- Kolokythas K., O'Sullivan E., Intema H., Raychaudhury S., Babul A., Giacintucci S., Gitti M., 2019, *MNRAS*, 489, 2488
- Kolokythas K., Vaddi S., O'Sullivan E., Loubser I., Babul A., Raychaudhury S., Lagos P., Jarrett T. H., 2022, *MNRAS*, 510, 4191
- Krabbe A. C., Oliveira C. B., Zinchenko I. A., Hernández-Jiménez J. A., Dors O. L., Hägele G. F., Cardaci M. V., Telles N. R., 2021, *MNRAS*, 505, 2087
- Kumari N., Maiolino R., Belfiore F., Curti M., 2019, *MNRAS*, 485, 367
- Liang L., Durier F., Babul A., Davé R., Oppenheimer B. D., Katz N., Fardal M., Quinn T., 2016, *MNRAS*, 456, 4266
- López-Sánchez Á. R., Westmeier T., Esteban C., Koribalski B. S., 2015, *MNRAS*, 450, 3381
- Loubser S. I., Babul A., Hoekstra H., Mahdavi A., Donahue M., Bildfell C., Voit G. M., 2016, *MNRAS*, 456, 1565
- Loubser S. I., Hoekstra H., Babul A., O'Sullivan E., 2018, *MNRAS*, 477, 335
- Loubser S. I., Lagos P., Babul A., O'Sullivan E., Jung S. L., Olivares V., Kolokythas K., 2022, *MNRAS*, 515, 1104
- Marino R. A. et al., 2013, *A&A*, 559, A114
- Martin P., Roy J.-R., 1992, *ApJ*, 397, 463
- McCarthy I. G., Frenk C. S., Font A. S., Lacey C. G., Bower R. G., Mitchell N. L., Balogh M. L., Theuns T., 2008, *MNRAS*, 383, 593
- McDonald M., Veilleux S., Rupke D. S. N., Mushotzky R., 2010, *ApJ*, 721, 1262
- McDonald M., Veilleux S., Mushotzky R., 2011, *ApJ*, 731, 33
- McDonald M., Veilleux S., Rupke D. S. N., 2012, *ApJ*, 746, 153
- Mernier F. et al., 2017, *A&A*, 603, A80
- Molina M., Eracleous M., Barth A. J., Maoz D., Runnoe J. C., Ho L. C., Shields J. C., Walsh J. L., 2018, *ApJ*, 864, 90
- O'Sullivan E. et al., 2012, *MNRAS*, 424, 2971
- O'Sullivan E., David L. P., Vrtilek J. M., 2014, *MNRAS*, 437, 730
- O'Sullivan E., Combes F., Hamer S., Salomé P., Babul A., Raychaudhury S., 2015, *A&A*, 573, A111
- O'Sullivan E. et al., 2017, *MNRAS*, 472, 1482
- O'Sullivan E. et al., 2018, *A&A*, 618, A126
- O'Sullivan E., Combes F., Babul A., Chapman S., Phadke K. A., Schellenberger G., Salomé P., 2021, *MNRAS*, 508, 3796
- Oliva-Altamirano P. et al., 2014, *MNRAS*, 440, 762
- Olivares V. et al., 2019, *A&A*, 631, A22
- Olivares V. et al., 2022, *A&A*, preprint ([arXiv:2201.07838](https://arxiv.org/abs/2201.07838))
- Osterbrock D. E., Ferland G. J., 2006, *Astrophysics of Gaseous Nebulae and Active Galactic Nuclei*, 2nd edn. University Science Books, Sausalito, CA
- Pagotto I., Krajnović D., den Brok M., Emsellem E., Brinchmann J., Weilbacher P. M., Kollatschny W., Steinmetz M., 2021, *A&A*, 649, A63
- Papaderos P. et al., 2013, *A&A*, 555, L1
- Parkash V., Brown M. J. I., Jarrett T. H., Fraser-McKelvie A., Cluver M. E., 2019, *MNRAS*, 485, 3169
- Phillips M. M., Jenkins C. R., Dopita M. A., Sadler E. M., Binette L., 1986, *AJ*, 91, 1062
- Pipino A., Kaviraj S., Bildfell C., Babul A., Hoekstra H., Silk J., 2009, *MNRAS*, 395, 462
- Polles F. L. et al., 2021, *A&A*, 651, A13
- Rennehan D., 2021, *MNRAS*, 506, 2836
- Rennehan D., Babul A., Hopkins P. F., Davé R., Moa B., 2019, *MNRAS*, 483, 3810
- Russell H. R. et al., 2016, *MNRAS*, 458, 3134
- Sánchez S. F., 2020, *ARA&A*, 58, 99
- Sánchez S. F. et al., 2012, *A&A*, 538, A8
- Sánchez S. F. et al., 2014, *A&A*, 563, A49

- Sánchez-Menguiano L. et al., 2018, *A&A*, 609, A119
 Sarzi M. et al., 2006, *MNRAS*, 366, 1151
 Sarzi M. et al., 2010, *MNRAS*, 402, 2187
 Schawinski K., Thomas D., Sarzi M., Maraston C., Kaviraj S., Joo S.-J., Yi S. K., Silk J. 2007, *MNRAS*, 382, 1415
 Scheneider P., 2006, *Extragalactic Astronomy and Cosmology An Introduction*. Springer, Berlin, Heidelberg
 Schindler S., Diaferio A., 2008, *Space Sci. Rev.*, 134, 363
 Schlafly E. F., Finkbeiner D. P., 2011, *ApJ*, 737, 103
 Serra P. et al., 2012, *MNRAS*, 422, 1835
 Shapiro K. L. et al., 2010, *MNRAS*, 402, 2140
 Sparks W. B., Macchetto F., Golombek D., 1989, *ApJ*, 345, 1
 Starkenburg T. K., Sales L. V., Genel S., Manzano-King C., Canalizo G., Hernquist L., 2019, *ApJ*, 878, 143
 Stasińska G. et al., 2008, *MNRAS*, 391, L29
 Taylor J. E., Babul A., 2001, *ApJ*, 559, 716
 Temi P., Amblard A., Gitti M., Brighenti F., Gaspari M., Mathews W. G., David L., 2018, *ApJ*, 858, 17
 Tremblay G. R. et al., 2018, *ApJ*, 865, 13
 Trinchieri G., di Serego Alighieri S., 1991, *AJ*, 101, 1647
 Valdes F., Gupta R., Rose J. A., Singh H. P., Bell D. J., 2004, *ApJS*, 152, 251
 van den Bosch R. C. E., Gebhardt K., Gültekin K., Yıldırım A., Walsh J. L., 2015, *ApJS*, 218, 10
 van Zee L., Salzer J. J., Haynes M. P., ODonoghue A. A., Balonek T. J., 1998, *AJ*, 116, 2805
 Voit G. M., Donahue M., 1990, *ApJ*, 360, L15
 Voit G. M., Donahue M., Slavin J. D., 1994, *ApJS*, 95, 87
 Weillbacher P. M. et al., 2020, *A&A*, 641, A28
 Werk J. K., Putman M. E., Meurer G. R., Santiago-Figueroa N., 2011, *ApJ*, 735, 71
 Werner N., Böhringer H., Kaastra J. S., de Plaa J., Simionescu A., Vink J., 2006, *A&A*, 459, 353
 Werner N. et al., 2014, *MNRAS*, 439, 2291
 Westmoquette M. S., Clements D. L., Bendo G. J., Khan S. A., 2012, *MNRAS*, 424, 416
 Yan R., Blanton M. R., 2012, *ApJ*, 747, 61
 Zezas A., Birkinshaw M., Worrall D. M., Peters A., Fabbiano G., 2005, *ApJ*, 627, 711

SUPPORTING INFORMATION

Supplementary data are available at [MNRAS](https://www.mnras.org/) online.

Appendix A. Other emission line galaxies in our MUSE data cubes.

Appendix B. Ha+[N II] $\lambda\lambda$ 6548,6584 emission-line maps.

Appendix C. Emission line ratio maps and BPT diagrams of the galaxies.

Appendix D. [N II] λ 6584 velocity fields.

Appendix E. [S II] λ 6716 / [S II] λ 6731 ratio maps.

Appendix F. Results of the linear fitting to data shown in Fig. 12.

Appendix G. Cold gas content.

Please note: Oxford University Press is not responsible for the content or functionality of any supporting materials supplied by the authors. Any queries (other than missing material) should be directed to the corresponding author for the article.

This paper has been typeset from a $\text{\TeX}/\text{\LaTeX}$ file prepared by the author.